MEDICAL ROBOTS

# Soft robotic steerable microcatheter for the endovascular treatment of cerebral disorders

**Tilvawala Gopesh[1], Jessica H. Wen[2], David Santiago-Dieppa[3], Bernard Yan[4], J. Scott Pannell[3], Alexander Khalessi[3], Alexander Norbash[5], James Friend[1,6]***



**Catheters used for endovascular navigation in interventional procedures lack dexterity at the distal tip. Neuro-interventionists, in particular, encounter challenges in up to 25% of aneurysm cases largely due to the inability to steer and navigate the tip of the microcatheters through tortuous vasculature to access aneurysms. We overcome this problem with submillimeter diameter, hydraulically actuated hyperelastic polymer devices at the distal tip of microcatheters to enable active steerability. Controlled by hand, the devices offer complete 3D orientation of the tip. Using saline as a working fluid, we demonstrate guidewire-free navigation, access, and coil deployment in vivo, offering safety, ease of use, and design flexibility absent in other approaches to endovascular intervention. We demonstrate the ability of our device to navigate through vessels and to deliver embolization coils to the cerebral vessels in a live porcine model. This indicates the potential for microhydraulic soft robotics to solve difficult access and treatment problems in endovascular intervention.**



## INTRODUCTION

About 1 in 50 people in the United States have an unruptured intracranial aneurysm, a thin-walled blister-like lesion on a cerebral artery that is prone to rupture. Studies estimate that cerebral aneurysms affect more than 160 million people worldwide (*1*, *2*), are increasing by more than 5%/year (*3*), and are responsible for 500,000 deaths per year worldwide; half the victims are younger than 50 (*4*). Annually, there are 30,000 new brain aneurysm ruptures in the United States alone (*5*). Cerebral aneurysms and their consequent long-term medical complications impose an enormous direct economic burden of $500 million per year in the United States (*6*). Intervention for unruptured aneurysms is generally known to be beneficial (*7*); without treatment, more than 50% of aneurysms larger than 5 mm eventually rupture and bleed (*8*, *9*). Of patients that suffer ruptured aneurysms, more than half die (*10*, *11*), and half the survivors experience long-term disabilities. The majority of aneurysms occur in vessels of 1.5 mm in diameter or less (*12*).

Cerebral aneurysm treatment was limited to invasive surgical clipping until the clinical adoption of endovascular coil embolization in the 1990s (*13*–*15*). A minimally invasive approach, i.e., coil embolization, involves inserting a microcatheter at the femoral artery, navigating it through tortuous vessel anatomy under radiological guidance to the aneurysm via the aortic arch and carotid arteries and deploying detachable coils into the aneurysm. The coils occlude the aneurysm from blood flow, inducing embolization. Endovascular coiling is now the most preferred (*16*), relatively cost-effective, and statistically more successful option for treating cerebral aneurysms (*17*, *18*).

Catheters are the primary tool used for treating vascular pathologies such as cerebral aneurysms via endovascular approaches. Although catheter technology has improved over the past few decades with notable advancements in pushability (*19*) and polymer coatings (*20*), the inability to steer the catheter tip in vivo remains (*21*). This complicates the navigation of tortuous anatomy, access into geometrically complex vascular pathologies that occur with aneurysms, and placement of the catheter tip in a stable position while deploying coils, stents, or sophisticated implants. Current gold-standard aneurysm embolization procedures use curved-tip guidewires to provide access via a previously introduced guidewire into aneurysm geometries that require acute catheter turns from the parent artery. However, upon retrieval of the guidewire in preparation to deliver coils, the catheter tip bends back to its original curvature, preventing coil deployment in the desired optimal direction.

The emergence of robotic-assisted surgical laparoscopic tools in the early 2000s—for example, the well-established, widely accepted Da Vinci system (*22*–*24*)—demonstrates that robotic actuators can beneficially augment a surgeon's dexterity in complex minimally invasive procedures. Likewise, the development of robotic tools for endoscopy and bronchoscopy has improved navigation and visualization of the gastrointestinal tract and pulmonary airways (*25*) and enabled advanced intervention for microscale suturing during such procedures (*26*). Although now widely used in abdominal and thoracic surgeries that permit >1-mm endoluminal systems, steerable catheter systems have not yet been widely adopted in endovascular neuro-interventions.

Fabrication methods have advanced over the last half century to enable machining arbitrary shapes to the microscale. Progress in photolithography, nanoimprint lithography, two-photon lithography to electron-beam lithography, and ion-beam machining have enabled the creation of massively parallel integrated semiconductor circuits, microelectromechanical devices, and micro- and nanofluidics. These technologies have revolutionized medical devices and practices (*27*, *28*). However, manufacturing arbitrarily shaped structures using hyperelastic materials at length scales between 10 μm and 1 mm remains a challenge because of the convergence of van der Waals, electrostatic, gravitational, and other forces of similar magnitudes at this scale, making machining and manufacturing difficult (*29*). Despite this, advancements in manufacturing methods have produced reductions in catheter diameters down to 1.8 Fr (600 μm). This has enabled endovascular techniques at more distal anatomical

[1]Department of Mechanical and Aerospace Engineering, University of California San Diego, La Jolla, CA, USA. [2]School of Medicine, University of California San Diego, La Jolla, CA, USA. [3]Department of Neurosurgery, University of California San Diego, La Jolla, CA, USA. [4]Melbourne Brain Centre, Royal Melbourne Hospital, Melbourne, VIC, Australia. [5]Department of Radiology, University of California San Diego, La Jolla, CA, USA. [6]Department of Surgery, University of California San Diego, La Jolla, CA, USA. *Corresponding author. Email: jfriend@ucsd.edu

locations, which is accompanied by increased tortuosity, additional bifurcations, and decreasing vessel diameters. This added complexity of distal vessel pathologies requires even more precise positioning for device deployment for effective treatment, requiring dexterous maneuvers by the interventionist (*21*, *30*, *31*). As a result, robotic-actuator assistance has grown to become a pressing unmet need in interventional procedures.

Here, we demonstrate how steerable endovascular microdevices can help address this clinical need, and how a combination of recent and classic microfabrication techniques can be used to produce these devices. Because of their hyperelastic and deformable nature, soft-bodied hydraulic actuators offer a combination of safety and ability in traversing tortuous routes to a treatment location to then treat the patient, all by performing complex hand-controlled miniature movements in the vasculature that would otherwise be impossible or require an invasive route. Among endovascular procedures, a subset of specialist procedures requiring access of small distal vessels that would benefit from dexterous locomotion of submillimeter diameter catheters are illustrated in Fig. 1.

Endovascular coil embolization of brain aneurysms in neurosurgery is a key example, and our approach provides a means of controllably orienting a catheter in cerebral arteries to deploy coils in tortuous anatomical locations. Before we describe our approach and the results of using it, we review past attempts to serve this need.

Magnetic approaches to catheter steering first proposed in the 1950s are constrained by magnetic field orientation, limitations of field saturation for small objects, and the complexity and cost of external field generation (*32*, *33*). Despite limitations (*34*, *35*), studies on magnetically driven micro- and nanorobots have made valuable contributions toward steerable actuators (*36*–*39*). Magnetic actuation has been combined with soft materials to demonstrate microscale flagella (*40*), tunable microstructures (*41*), and externally controlled continuum soft robots (*42*). Magnetically driven steering has been demonstrated to be effective in cardiac electrophysiology procedures (*43*–*45*). However, implementation requires costly infrastructure such as magnetic resonance imaging magnets, robotic arms, and external control systems (*46*).

Pull-wire systems, based on the Bowden cable technique, were proposed as a means of catheter steering in the 1960s (*47*–*51*). Wires run from the proximal end of the catheter to the distal tip where a deflection can be achieved based on the push or pull motion of the cables. These range from single cable systems for unidirectional deflection (*52*) to multisegment (*53*) for dual directional control. Pull-wire systems are hampered by inevitable undesired torsion (*54*), buckling (*55*), internal friction (*19*), and external friction (*56*, *57*). These factors, and the stiffening often used to avoid them, can independently or together result in undesired tip motion resulting in vascular damage (*58*–*60*).

Piezoelectric ultrasonic approaches (*61*, *62*) have also been proposed but currently face practical reliability and safety challenges. Using vibration transmitted across a contact interface to a steerable component, the devices are liable to lose the steerable component or exhibit unanticipated motions when in contact with the vascular wall. They also require 1 MHz or greater frequency oscillating electrical signals to be transmitted to the distal tip; neither wired nor wireless methods are able to do this to date.

The burgeoning field of soft robotic methods drawing deformable materials into bioinspired three-dimensional (3D) structures has seen growth in research and applied technology (*63*–*67*) ranging from anatomical replacements such as prosthetic limbs to surgical tools (*68*–*72*). Studies have demonstrated the use of soft robotics in balloon catheters with electrophysiological and ablation capabilities (*73*) and in implantable soft robotic sleeves to support heart function (*74*). Soft robotic–based hydraulic and pneumatic actuators first proposed in the 1990s (*75*–*77*) include pressure-driven motion (*78*), vacuum-driven motion (*79*), and hydraulic jets (*80*). Through newer fabrication capabilities, smaller soft robotic structures with unidirectional motion (*81*) and more complex larger scale soft robotic structures with untethered actuation capabilities (*82*) have been presented.

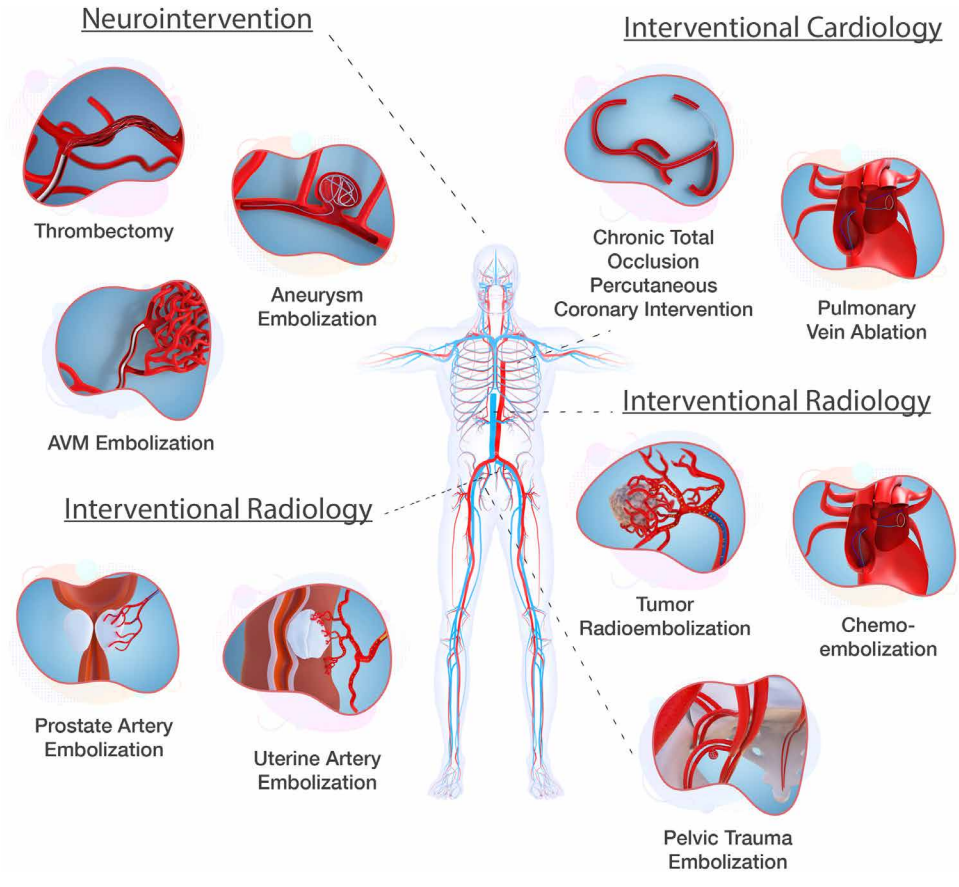


**Fig. 1. Endovascular procedures that would benefit from submillimeter diameter steerable catheters.** Aneurysm embolization is the focus of this paper, but steerable submillimeter catheters are broadly useful across the human vasculature.

There are more than eight hundred patents that describe methods of enabling steering at the distal end of a catheter tip (*21*, *30*). A small number of these that use magnetic (*83*, *84*) and pull-wire systems (*85*) are commercially available but at diameters greater than 1 mm. For clinical use, a microcatheter must be radio-opaque to be visible during a procedure and have a central lumen with a lubricious coating to permit the smooth passage of guidewires and implants. The ability to actively steer, navigate, position, and deploy sophisticated implants such as coils, flow diverters, stents, or glue does not exist at these scales today.

Here, we present a soft polymer tip distally attached to a 1.6-m catheter with a contiguous lumen. Because balloon catheters—representing a crude form of hydraulic soft robotics—are broadly accepted as safe and effective in endovascular intervention, a hydraulically actuated fully steerable microcatheter can reasonably be expected to be similarly safe and effective if the pressures used are similar or less. The tip in our device is hydraulically steered via four 50-μm-diameter cylindrical, saline-filled channels, in part inspired by highly deformable microscale mechanisms observed in nature (*86*). These axially oriented channels are equally spaced around the catheter wall for hydraulic actuation. Pressurizing one or more of these channels produces an internal stress that creates an axial differential strain and an associated deflection and thus "steers" the tip away from the pressurized channel(s) in a desired direction (*87*). Although there is also radial and azimuthal internal stress from the pressure, the structure is specifically designed to minimize radial expansion and promote axial deformation, unlike balloon catheters. This prevents inward expansion to potentially constrict and clamp whatever may be in the internal lumen or outward expansion to potentially occlude the vessel or damage the arterial endothelium.

The steerable tip was fabricated using a simple but effective laboratory-based technique to manufacture submillimeter-scale high-aspect ratio structures with hyperelastic materials (detailed in Materials and Methods). Both the inner lumen and outer surface of the catheter were coated with a hydrophilic coating to reduce friction between the microcatheter and the endothelial walls of the arteries and between the microcatheter and devices such as coils passed within the lumen. The tip was assembled with 160-cm-long catheter-grade tubing connected to a handheld controller to form a closed-system, stand-alone microcatheter with a steerable tip that can be used independent of external controllers, robotic arms, or additional infrastructure.

We demonstrate the use of the active steering capability of this microcatheter device in navigating through tortuous cerebral vasculature and in deploying coils to treat cerebral aneurysms in a representative ex vivo model. The results and interventionist feedback from testing in the ex vivo model were used to iteratively improve the device design to eventually produce a device suitable for in vivo testing. A representative in vivo endovascular coiling procedure was conducted in live porcine. Contrary to conventional wisdom that tethered microactuation at the high length-to-diameter aspect ratios required in medical applications—10,000:1 in our case—would be impractical because of viscous losses, we demonstrate that well-designed structures with engineered hyperelastic materials can enable seamless real-time control of microscale soft-bodied robots via 1.5-m-long, 50-μm-diameter microfluidic channels.

## RESULTS

### A hydraulically actuated soft robotic steerable tip at dimensions compatible with cerebral arteries

As previously noted, a majority of cerebral aneurysms occur in vessels less than 1.5 mm in diameter (*12*). Cerebral arteries supplying blood to the brain begin above the neck, at the base of the internal carotid artery (ICA) through to the middle cerebral artery (MCA) bifurcation, and next branching to smaller and more tortuous cerebral vessels. The MCA has a diameter of about 2.6 mm (Fig. 2A) (*88*); blood vessel branches beyond the MCA gradually decrease in size to a diameter of 1 mm or less (*89*). To navigate smoothly within cerebral vessels, current gold-standard microcatheters have an outer diameter of 900 μm (3 Fr) and an inner diameter of 400 μm (1.2 Fr) to provide a lumen for guidewires, detachable coils, and sophisticated

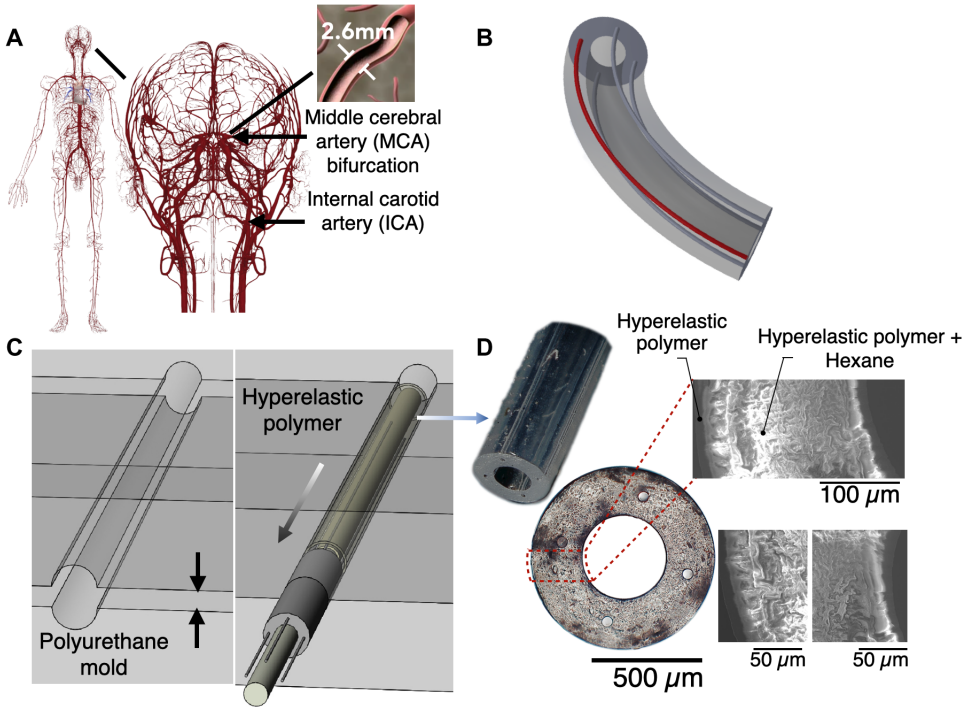


**Fig. 2. Engineering a steerable catheter.** (**A**) Illustration of the cerebral arterial structures and the average diameter of the MCA. [Image courtesy of Complete Anatomy, with thanks to @3D4Medical] (**B**) Design and working principle of the hydraulically driven tip: When a channel is inflated (indicated in red), the tip deflects in the opposite direction. (**C**) Fabrication of the catheter is a multistep molding process. (**D**) Plan and cross-section images of the as-fabricated steerable tip tubing with a length of 15 mm, an outer diameter of 900 μm, an inner diameter of 400 μm, and four 50-μm channels in the tube wall. The relatively rigid coating upon the softer interior material that forms the hydraulically driven tip is visible via scanning electron microscope cross-sectional images and is about 25 μm thick.

endovascular devices such as stents and flow diverters. To provide clinical compatibility and immediate familiarity when used in existing procedures, the steerable tip microcatheter described here was designed to have an outer diameter of 900 μm, enclosing four 50-μm-diameter channels for hydraulic actuation and a 400-μm-diameter central lumen. Upon inflating one of the 50-μm-diameter channels, an axial differential strain is induced in the structure about its midplane—the axis of symmetry along the length of the tip—causing bending of the tip away from the inflated channel (Fig. 2B). The fabrication of the steerable tip is illustrated in Fig. 2; details are provided in Materials and Methods. A mesoscale molding process using thin wires cast with silicone rubber in polyurethane plastic molds (Fig. 2C) was used.

### The steerable tip is engineered to limit radial expansion and promote bending

Unlike the use of saline injection into catheter tips to radially inflate balloons to pin a catheter and to deploy and expand a stent, avoiding radial expansion of the fluid-filled channels is important in our device. This was achieved by carefully designing the placement and size of the fluid channels and by cocasting concentric layers of a platinum-cure hyperelastic silicone rubber (Dragon Skin 10 SLOW, Smooth-On Inc., Macungie, PA USA; details are provided in Materials and Methods).

### Choosing the radius and radial location of the hydraulic channels

Although the inner and outer diameters of the steerable microcatheter tip are inherently constrained by the diameter of the cerebral arteries (*88*) and designed to be commensurate with the dimensions of the existing gold standard microcatheters, producing a steerable tip without radial expansion required a design study focusing upon the radius ($R$) and radial position ($R_P$) of the hydraulic channels as parameters. Using a computational model, the radii for hydraulic input were varied from 25 to 100 μm while maintaining a fixed radial position (325 μm from the center). The position of the hydraulic channel was varied from 260 to 390 μm from the center of the lumen while maintaining a fixed channel radius of 50 μm.

The number of channels also affects the device mechanics because a greater number of small channels could produce an improved ability to steer, but a key drawback in introducing more than three to four channels is the rapid increase in complexity of the tip-to-catheter and catheter-to-hand controller interfaces. Consequently, we limited our study to four channels and noted that three or fewer channels produce similar results, albeit with reduced functionality with two or fewer channels. Furthermore, the computational expense of accurately computing the nonlinear finite deformation of a nonlinearly (stiffening) elastic media in a structure with a length:width aspect ratio of 1:1000, together with practical fabrication limitations imposed by the small scale and intrinsic challenges in making such structures, limited our choices for the channel radius ($R$) and the radial position of the channel ($R_P$) to three values each. Even so, it is apparent from Fig. 3 (B and C) (and Fig. 4) that the range of choices considered has a marked effect on the performance of the device.

Furthermore, Fig. 3 (B and C, solid lines) plots the tip's curvature versus input pressure using image capture and postprocessing. The pressure required to achieve a curvature of 400 1/m (180° total bend, forming a "C" shape) is 350 kPa, nearly half the pressure used in traditional balloon catheters (600 kPa) (*90*) for stent deployment. Positioning the radius away from the midpoint of the wall thickness results in inadequate curvature at higher input pressures (Fig. 3B). The 50-μm-diameter channels exhibit 10% strain to achieve a 180° bend. The selected material produces a strain at failure >350% (*91*) at pressures 4× that required to achieve 10% strain. In the inadvertent case of overpressurizing the hydraulic channel, the steerable tip loops on itself at pressures higher than 350 kPa and will rupture at a pressure of 1200 kPa, thus providing a safety factor of ≈4.

Although a smaller channel radius of $R$ = 25 μm, for example, helps to reduce radial expansion (Fig. 4A), the bending curvature is reduced for the same input pressure (Fig. 3A). A larger radius, $R$ = 75 μm, produces greater curvatures at relatively lower input pressures (Fig. 3A), although radial expansion is also much greater (Fig. 3A). The large mismatch in the simulated results for the radial expansion indicates that, initially, the hydraulic channels rapidly expand and reach a maximum saturation point where the concentric layers prevent further expansion. As the hydraulic channels elongate, the radial expansion reduces to compensate. Although the experimental results demonstrate a similar trend, it is more subtle than the simulated results. Whereas the concentric layers prevent excess radial expansion at the required curvatures, the elongation

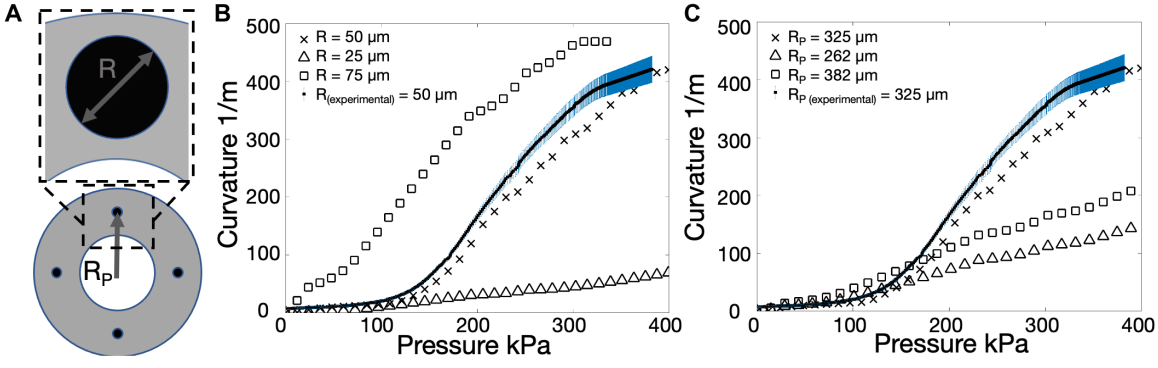


**Fig. 3. Design parameters of the steerable tip and the consequent curvature as a function of input pressure.** Nonlinear finite deformable structural mechanics analysis was used to compute the relationship between the tip curvature and input pressure for three values of (**A**) the channel radius ($R$) and the channels' radial position ($R_P$). (**B** and **C**) The curvature of the tip as a function of the input pressure produces substantially different computational results for the (B) radius $R$ with the radial position $R_P$ at $R_P$ = 325 μm and (C) radial channel position $R_P$ for a channel radius $R$ = 50 μm. The computed results are similar to [solid line in (B) and (C)] experimental results obtained with $R$ = 50 μm and $R_P$ = 325 μm. The experimental results are averaged for four channels; blue lines indicate error bars (SD).

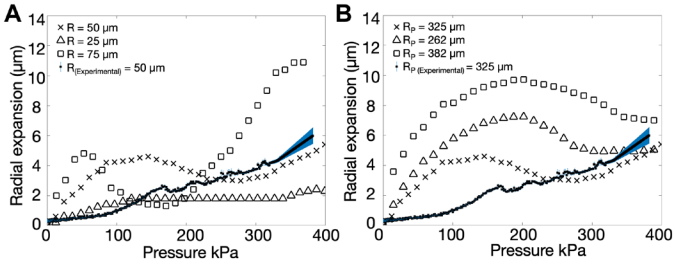


**Fig. 4. The hydraulic channels' position and radius affects the relationship between the tip's radial expansion and the input pressure.** Computed radial expansion of the steerable tip at its outer surface as a function of (**A**) channel radius $R$ with $R_P = 325$ μm and (**B**) channel radial position $R_P$ with channel radius $R = 50$ μm compared with experimental results for a tip with $R = 50$ μm and $R_P = 325$ μm. The experimental results are averaged for four channels; blue lines indicate error bars (SD).

during the experiment does not cause a reduction in the hydraulic channel radius.

### Tailoring the tip's construction to further reduce radial expansion

The innermost and outermost surfaces are made with the hyperelastic polymer, whereas the region enclosed by these surfaces is formed from a relatively softer 1:1 mixture by weight of the hyperelastic polymer with hexane (95% anhydrous hexane; CAS 110-54-3, Sigma-Aldrich, St. Louis, MO USA).

The purpose of this layering and the placement and sizing of the fluid channels is to promote axial deformation while minimizing radial expansion. The key is to observe that the layering of different hyperelastic materials induces stress-stiffening (*91*). Consequently, the introduction of a pressure in one of the channels produces radial, axial, and azimuthal stress, and as these values increase, the rate of strain increase gradually falls. The radial strain, over the relatively short length scale of the wall thickness of the catheter tip, quickly reaches the stiffening portion of the hyperelastic stress-strain response.

However, because the tip is ~100 times longer than its radius, the axial deformation is likewise ~100 times greater than the radial deformation for the same strain value. The axial deformation is therefore far greater, producing ample bending of the tip with negligible radial expansion. This material choice is contrary to the choice of strain-softening hyperelastic media typical in balloons. Further, the relative rigidity of the polymer without hexane treatment serves as a constraint to radial expansion, squeezing the relatively soft hexane-treated polymer within to axially exude from the channel pressure. Catheter tips made without layering exhibit substantially larger radial expansion (Fig. 8).

### Forming full-length (160 cm) catheters

The soft polymer tip with a 400-μm-diameter central lumen and 50-μm-diameter hydraulic channels at a radial position $R_P = 325$ μm was attached end to end to long catheter-grade and matched multibore tubing (as detailed in Materials and Methods) to produce 160-cm-long catheters that mimic current microcatheters used in clinical treatment of cerebral aneurysms. Pebax, a copolymer made of polyamide and soft polyether used in the majority of commercially available catheters, was used in the multibore tubing with graduated stiffness along its length. For the larger and stiffer femoral artery and aorta, high and medium durometer Pebax were used for the proximal catheter, whereas lower durometer Pebax was used for the distal catheter passing through the smaller and more fragile cerebral arteries.

### Biplane x-ray visible radiopacity

To ensure the steerable tip is visible via digital biplane x-ray typical in interventional angiography suites, gold radiopaque markers (27121A, Johnson Matthey, San Diego, CA, USA) were embedded in the soft polymer tip. Markers are positioned at three distinct locations. The first and second markers indicate the beginning and end of the steerable portion of the microcatheter tip. The third marker, the most proximal, is located 3 cm from the distal end of the catheter tip and aligns with the marker on the coil pusher of an embolization coil. This third marker aids in visualization of the point at which an entire coil has been deployed into an aneurysm, indicating that the pusher should not be further advanced. This marker could be similarly used for other types of devices, including flow diverters or stents that may be placed in the lumen of the microcatheter. The remainder of the nonsteerable portion of the catheter was made with standard barium-filled Pebax tubing to achieve clinically required radiopacity.

### Reducing friction between the inner lumen and guidewires and coils

To overcome friction between the catheter's inner lumen and devices such as stents or coils as well as friction between catheters and the surrounding vessel, commercial catheters have hydrophilic coatings on the inner lumen. This provides a lubricious passageway for devices and on the exterior to reduce the risk of damage to the vascular endothelium and to avoid vasospasm (*92*). The exterior coating furthermore reduces sudden release of built up forward pressure accumulated in frictional contact between the catheter and vascular wall at multiple vascular bends. As catheters are advanced, frictional resistance on the outer catheter surface at these bends may clamp it and cause it to accumulate elastic energy that can be suddenly and unpredictably released to pop the distal portion of the catheter forward, potentially resulting in catastrophic vessel dissection or aneurysm rupture. Silicone rubbers similar to those used in this study are known to exhibit unacceptably large surface friction (*93*). To reduce this friction, we used a hydrophilic coating (ON-470, Aculon Inc., San Diego, CA, USA) to achieve smooth advancement and navigation of our microcatheter through both ex vivo and in vivo models and the smooth advancement of coils through the microcatheter lumen.

### An ex vivo model to provide practice and feedback in treating cerebral aneurysms with this system

Performance of the steerable catheter was assessed and iteratively improved through testing by clinical practitioners in ex vivo silicone models representative of the human vasculature and similar to models used to test commercially available catheters (*94*–*96*). A single vasculature model of vessels from the femoral artery to the ICA, including the aortic arch, was constructed. Anonymized computed tomography (CT) angiogram DICOM (Digital Imaging and Communications in Medicine format) images from a patient with representative vessel geometry were segmented, 3D-printed, and used to fabricate a representative model using silicone rubber as shown in Fig. 5 (details are provided in Materials and Methods). A separate silicone phantom

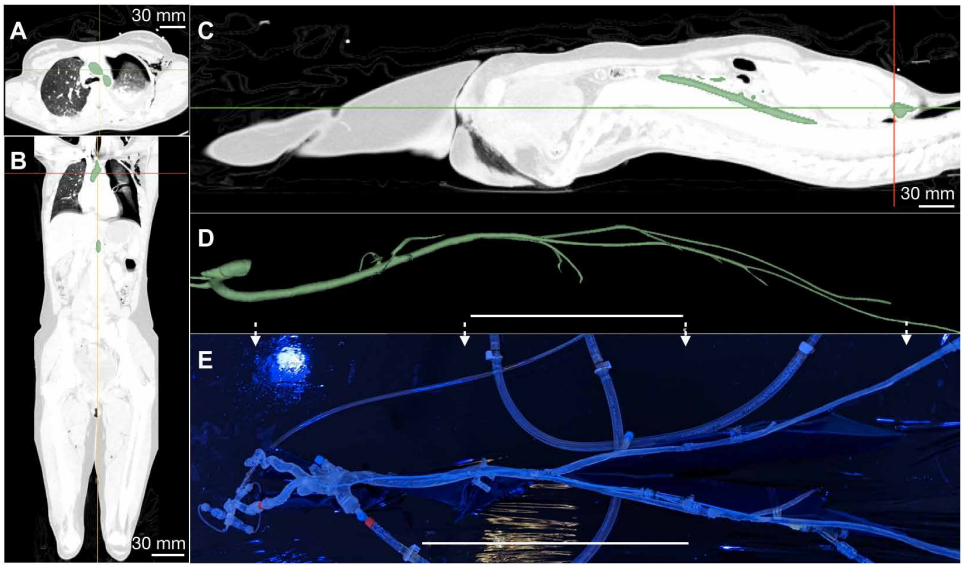


**Fig. 5. Fabrication of an ex vivo silicone model from anonymized patient data.** (**A**) Axial, (**B**) sagittal, and (**C**) coronal views of CT angiogram images with vascular segmentation for a single slice shown in green. This process produces a (**D**) complete vascular model from the femoral artery to the aortic arch, including principal vascular branches, particularly the carotid arteries to the cerebrovasculature. Through 3D printing and lost ABS casting as detailed in the text, (**E**) a functional, fluid-tight vascular model may be produced. Scale bars, (D and E) 25 cm.

from the internal carotid to the cerebral vessels including the aneurysm was fabricated using the same approach; the aneurysm presented here was selected to represent a challenging geometry at the posterior communicating artery (PCOM) requiring acute angle turns. The primary factors iteratively improved include transitional stiffness, friction, and radio-opacity.

### Neuroendovascular surgical setup commensurate with clinical procedures

Using the right femoral artery of the silicone model as the access point, a guide catheter was inserted into the silicone model; the distal end of the larger guide catheter was parked at the mid-ICA. Standard saline was used to flush the guide catheter and microcatheter in line with standard endovascular neurosurgical protocols (*97*). Unlike conventional endovascular neurosurgery, once the guidewire was used to reach the aneurysm location in tandem with the microcatheter, the guidewire was retrieved and the hydraulic actuation of the steerable catheter engaged to direct the distal end of the steerable tip into the dome of the aneurysm was then used to lock the tip at the geometric center of the aneurysm. Detachable coils were introduced through the hub of the steerable microcatheter and deployed into the aneurysm dome (movie S2).

### Testing in vivo in porcine

A skeletally mature (47 kg) female pig underwent general endotracheal anesthesia. Cardiorespiratory monitoring was performed throughout the procedure under the supervision of a veterinary technician. Details are provided in Materials and Methods.

Referring to Fig. 6, after surgical exposure, a 6-Fr sheath was placed in the left femoral artery using the modified Seldinger technique (*98*). Under roadmap fluoroscopic guidance, a 5-Fr guide catheter was advanced to the right common carotid artery (CCA) over a 889 μm guidewire. The 889 μm guidewire was retrieved. A straight 355.6-μm microwire was inserted into the soft-robotic steerable catheter, and the microsystem was then advanced to the distal end of the guide catheter. The 355.6-μm microwire was retrieved, and the hydraulic actuation of the steerable catheter was engaged to traverse from the external carotid artery to the ascending pharyngeal artery. Hydraulic actuation was disengaged, returning the tip to its native, straight orientation. The steerable microcatheter was further advanced, and the hydraulic actuation, applied by pressurizing saline through a 1-ml syringe, was then engaged to direct the distal end into the parotid artery. The steerable tip was locked in a fixed curvature position using a one-way stopcock, and detachable coils were deployed via the hub of the microcatheter (see movies S3 and S4).

## DISCUSSION

Here, we introduce the design and fabrication of a hydraulically actuated soft robotic microcatheter and demonstrate its ability to steer in a pig model and enable deployment of coils in complex anatomical geometries with acute angles.

Although more than 50% of intracranial aneurysms are treated via endovascular coiling, the efficacy and outcomes of endovascular aneurysm embolization are still inferior to traditional invasive clipping (*99*). The difficulty in navigating a microcatheter through tortuous vasculature, directing the catheter tip to the aneurysm dome, and holding it in a stable position accounts for many coil embolization procedure failures. These include incomplete aneurysm occlusion (*100*), aneurysm recanalization (*101*), coil malposition (*102*), and intraoperative rupture (*103*, *104*). These failures can be attributed to unfavorable vessel tortuosity and aneurysm geometry. Furthermore, up to 25% of intracranial aneurysms cannot be endovascularly treated, often due to aneurysm location—where the vessel is too difficult to reach—or geometry—where the dome, neck, or angles are unfavorable for microcatheter cannulation or coil support. Up to 25% of surgical neurointerventions fail in attempted endovascular treatment of intracranial aneurysms (*99*, *100*). The ability to treat aneurysms of unfavorable shape and size and the durability of embolization coils in the dome after intervention remain challenges in the endovascular coiling technique (*101*).

In cases of severe carotid system tortuosity, intracranial positioning of microcatheters to access the aneurysm dome may be impossible or hazardous. In tortuous or fragile vasculature, turns of 180° and 360° are particularly difficult, catheterization often requires multiple attempts, and vasospasms are often induced (*92*). Tortuous arterial anatomy forces microcatheters along the outer curvature of the vessels at each turn, creating stresses on the vessel, a potential mechanism for vessel dissection (*105*). Furthermore, minimizing the overall procedure time is important not only to minimize costs but also to avoid excessive x-ray fluoroscopy exposure and associated risks such as thromboses or tumor growth (*106*–*108*).

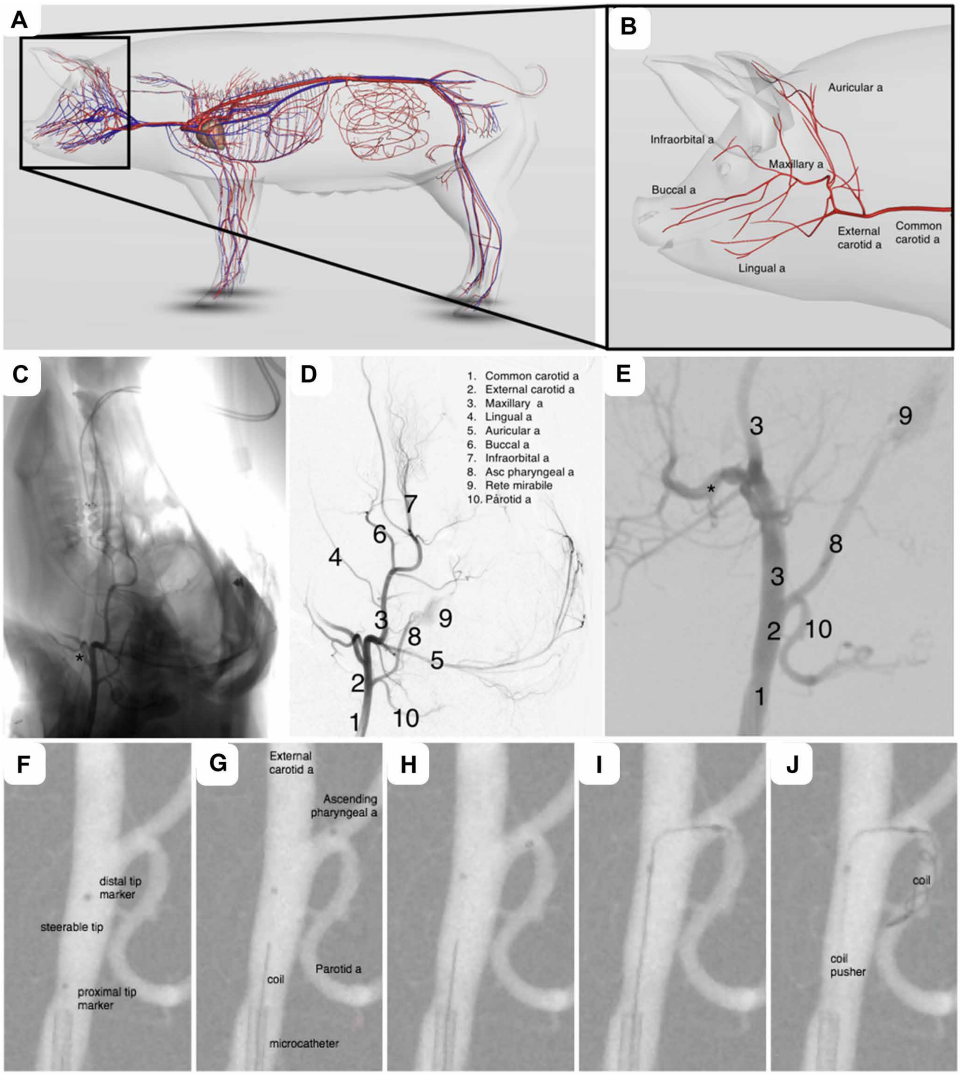


**Fig. 6. Animal study.** Illustration of porcine (**A**) arteries and (**B**) cerebral arteries for reference. [Images courtesy of 3D Pig Anatomy Software by Biosphera] (**C**) Anteroposterior (AP) diagnostic subtraction angiogram of the right CCA. (**D**) Spot AP roadmap fluoroscopic image of the right CCA enlarged in (**E**). (**F**) Position one showing the steerable microcatheter before the introduction of a hydraulic load. (**G**) Position two showing the microcatheter after hydraulically steering the tip to access the ascending pharyngeal artery from the external carotid artery. (**H** and **I**) Position three showing the hydraulic steering of the catheter tip to access the parotid artery from the ascending pharyngeal artery. (**J**) Coils deployed in the parotid artery from the stabilized catheter tip.

To address the lack of steerability, catheter manufacturers provide 45°, 90°, and C-shaped tips in fixed orientations, and neurointerventionists will often retrieve, reshape, and reintroduce their microguidewire tips in hopes of accessing tortuous aneurysm geometries using a "trial and error" approach. Upon retrieval of the guidewires, the catheter tip will return to its native shape, and none of the catheters can be steered once inside blood vessels.

A microcatheter with a soft tip that can be controllably directed in an artery during endovascular coil embolization could decrease procedure time and reduce the failure rate of these procedures. Comparative studies between steerable and nonsteerable catheters have demonstrated reductions in procedure time and improvements in patient safety (*109*–*111*). Steerable catheters are known to enable better positioning of sophisticated implants (*112*, *113*) and successful treatment in patients who would otherwise be precluded from endovascular treatment with a standard nonsteerable catheter (*46*, *114*).

The work described here demonstrates the use and efficacy of a hydraulically actuated soft polymer tip that can be steered and locked in a desired position at the distal end of a microcatheter in vivo. A microcatheter with a steerable tip would allow safer and quicker navigation through tortuous anatomy, improved access of a more desirable target location relative to the aneurysm dome, and coil deployment with a more stable platform. Because of their inherent rigidity and size, traditional robotic tools would not be able to achieve this within blood vessels at the millimeter scale. Likewise, a purely soft material approach would present serious technical challenges with regard to pushability in vivo. Here, we leverage microfabricated soft robotic actuators with engineered hyperelastic materials to assemble full-length catheters with transitionally variable stiffness from the distal to proximal end. This device further enables the deployment of devices such as stents and flow diversion pipelines in challenging anatomical configurations. Although balloon-assisted coiling (*115*) has been used to mechanically assist in orienting a catheter tip in endovascular neurointervention procedures, this method does not provide control over catheter tip orientation within the aneurysm dome and, because of anatomical size constraints, cannot be used in smaller blood vessels.

In the present work, a steerable tip microcatheter at the submillimeter length scales commensurate with endovascular neurosurgical catheters was fabricated, characterized, and tested in ex vivo silicone models representative of the human vasculature. Feedback from practicing neurointerventionists was incorporated to iteratively improve device performance before conducting an in vivo trial in live porcine. Existing technology is unable to systematically provide access to arteries that are acutely joined to the parent artery where the catheter is located. Here, we have shown the ability to accomplish this difficult task with the steerable tip in vivo through the following steps (referring to Fig. 6 and movie S2):

1) Access the ascending pharyngeal artery from the external carotid artery.

2) Access the parotid artery from the ascending pharyngeal artery.

3) Maintain the acute turn position while deploying coils.

Furthermore, the reported steerable catheter demonstrated a higher level of safety than clinically experienced when using current

gold-standard catheters. An important risk of endovascular platforms is the mechanical injury to the vessel. This manifests as a vessel dissection and/or perforation that is immediately evident to the surgeon during follow-up angiograms performed during the procedure. Our catheter caused no injury to the endothelium or perforation of the vessel lumen on follow-up angiographic views as shown in Fig. 6 (F to J and movie S2). On the basis of these three characteristics, there is a reasonable basis to conclude that our catheter may provide a greater level of procedural safety relative to current gold-standard procedures. However, this still has to be verified through animal trials outside the scope of the present research effort.

The results include a demonstration of a guidewire-free navigation, access, and coil deployment procedure in cerebral blood vessels using a hydraulically actuated microcatheter. The main purpose of the in vivo model was to demonstrate our catheters' performance in physiologic conditions including temperature, blood pressure/pulse pressure variation, and the complex chemical composition (and prothrombotic characteristics) of live blood. This proof-of-concept experiment demonstrated that our catheter performed as intended.

On the basis of the resulting data, the technology demonstrates promise as a viable approach to augment the function of existing microcatheters in treatment of vascular injuries. Likewise, the present work demonstrates that recent fabrication approaches in combination with bioinspired motion can be used to pave the way for a set of tools useful for conducting autonomous vascular surgery, for instance, to specific locations inside the heart (*31*).

Although the present work focuses on treatment of aneurysms in cerebral blood vessels, the described steerable device can be extended to treat or diagnose a broader set of pathologies through application to other procedures that also require fine, dexterous manipulations. Similar challenges of small vessel diameter and complex vessel tortuosity in addition to vessel occlusions are encountered in interventional cardiology and general vascular surgery. Nonvascular applications include pulmonary nodule biopsy during bronchoscopy in interventional pulmonology, where an analogous branching airway system with progressively smaller branches also involves a navigational procedural challenge. The soft material steerable device presented here has the potential to facilitate a number of procedures that require submillimeter diameter catheters in other delicate surgical locations.

## MATERIALS AND METHODS

### Detailed description of the fabrication process

The process of fabricating the steerable catheter tip is complicated by the challenges of working at this scale and the need to produce a smooth, uniform, and fluid-tight multilayer structure. The basic procedure is illustrated in Fig. 7, starting with fabrication of the molds (Fig. 7, A to D), followed by mold alignment (Fig. 7, E and F), formation of the relatively stiff thin polymer films present on the inner and outer diameter of the steerable tip (Fig. 7, G to I), the alignment of metal rods as casting structures for the hydraulic passages (Fig. 7J), and, lastly, producing the steerable tip via casting (Fig. 7K) and demolding of the silicone rubber (Fig. 7, L and M). The capillary tubes and glass strips were bonded to the microscope slide using an ultraviolet (UV) light–cured epoxy (NOA60, Norland Inc., Cranbury, NJ, USA). The molding material, a two-part polyurethane plastic (Smooth-Cast 327, Smooth-On Inc., Macungie, PA, USA) selected for its hardness and smooth finish, was poured over the assembly and degassed. Upon curing, the polyurethane plastic was debonded from the glass tubing to produce one-half of the mold. Two halves were placed facing each other with a custom-manufactured glass capillary tube (Vitrocom Inc., Mountain Lakes, NJ, USA) between them for alignment with a vise to clamp the assembly. The

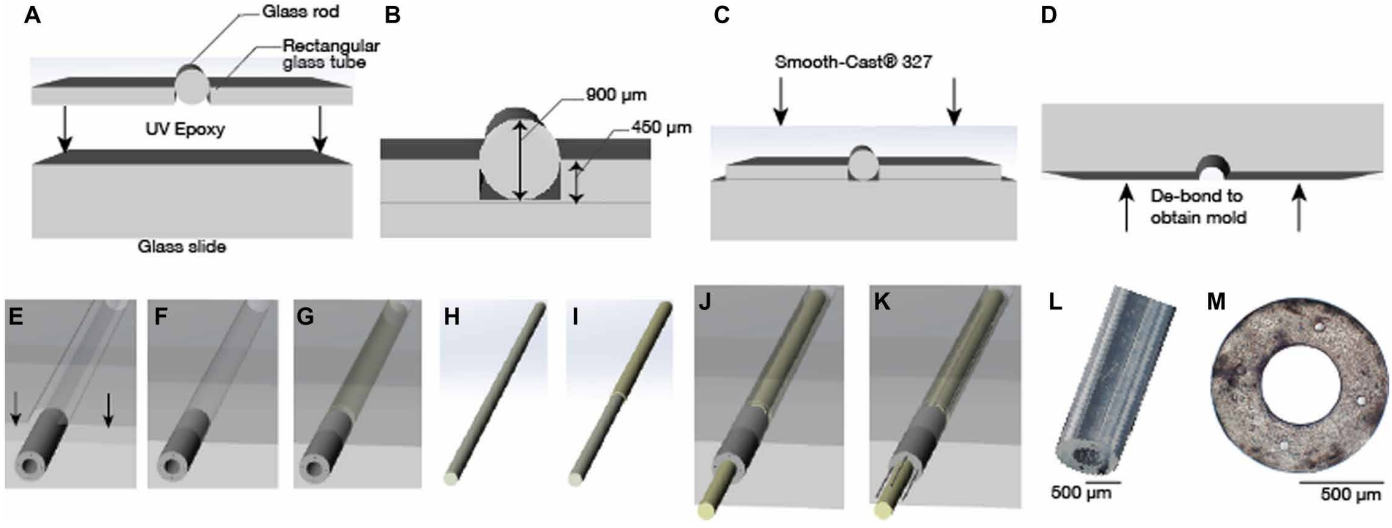


**Fig. 7. Steerable catheter tip fabrication process.** (**A**) Circular glass rods (diameter, 900 μm) were placed next to 450-μm-thick rectangular glass sheets and (**B**) bonded to a microscope glass slide using UV epoxy. (**C**) Smooth-Cast 327 was poured over the assembly and, upon curing, (**D**) debonded to obtain one-half of the complete mold. The mold is formed by (**E** and **F**) clamping two such halves facing each other with a custom glass capillary tube (outer diameter of 900 μm, inner diameter of 400 μm, and four 50-μm channels in the wall) to provide alignment. Relatively stiff Dragon Skin 10 SLOW is first injected into the mold and then blown out with air to produce a thin layer (**G**) on the inside of this mold. (**H**) A 400-μm glass capillary tube is likewise (**I**) spin-coated with the same material and (**J**) introduced into the mold with (**K**) four wires that represent the fluid passages for tip steering. The vacant regions are filled with Dragon Skin 10 SLOW mixed with Hexane. The result of this process is a (**L** and **M**) multilayer soft polymer structure.

900-μm optical density, 400-μm inside diameter glass capillary tube has four 60-μm channels in the wall for later introduction of wire that serve to mold the fluid passages used to steer the tip. Dragon Skin 10 SLOW (Smooth-On Inc., Macungie, PA, USA) was pumped into the mold to fill it. Dry compressed air at ~345 kPa was then blown through the mold to clear the mold, leaving a thin coating of Dragon Skin upon the mold surfaces.

Separately, a 400-μm-diameter glass capillary tube was coated with release agent [Ease Release205 (Smooth-On Inc., Macungie, PA, USA); see Fig. 7, H and I]. The tube was spin-coated with Dragon Skin 10 SLOW at 2000 rpm for 25 s and left to cure for 24 hours. The Dragon Skin 10–coated glass capillary tube was placed in the central lumen of the mold structure. Four 2% rhenium-tungsten rods (Mitaka Co., Saitama, Japan), 50 μm in diameter, chosen for their rigidity and smooth surface finish, were then passed through the capillary channels in the multibore glass capillary tube until they extended beyond the structure by 15 mm. Dragon Skin 10 SLOW, mixed with hexane (296090, Sigma-Aldrich, St. Louis, MO USA) in a 1:1 ratio, was degassed and pumped with a syringe through the open end of the mold to fill it. Once cured, the wires and 400-μm-diameter glass capillary tube were carefully withdrawn, leaving behind the cavities for the inflatable microchannels and the central lumen. The Smooth-Cast 327 molds easily detach from the silicone rubber to obtain a steerable tip (Fig. 7L) with precisely defined dimensions and microhydraulic channels (Fig. 7M).

### The multilayer structure of the polymer in the tip is important to avoid radial expansion

Without concentrically layering the outer and inner surfaces of the steerable tip with Dragon Skin to provide a relatively stiff surface upon the 1:1 Dragon Skin–hexane combination that forms the majority of the flexible tip material, the steerable tip exhibits radial expansion as indicated in Fig. 8. With the relatively soft 1:1 Dragon Skin–hexane combination alone ("Nonlayered"), the radial expansion is at least four times the layered structure of 1:1 Dragon Skin–hexane inside a thin film of Dragon Skin. The surface layer is about 25 μm thick as seen in Fig. 2D).

### Assembly of full-length devices with transitional stiffness

In each case, the 400-μm-diameter central lumen and 50-μm-diameter channels were tethered to a handheld controller through microtubing

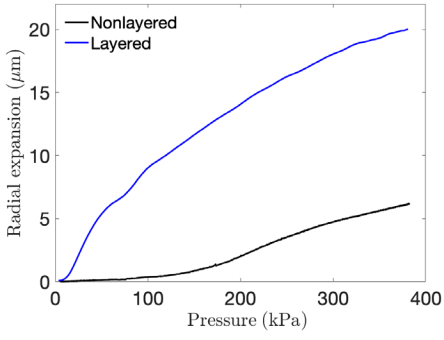


**Fig. 8. A thin coating of relatively stiff polymer reduces radial expansion.** Radial expansion of the steerable tip with and without a relatively stiff 25-μm-thick layer of Dragon Skin 10 SLOW upon Dragon Skin–hexane to form the bulk of the steerable tip structure. The steerable tip fabricated with concentric layers of Dragon Skin encompassed by Dragon Skin mixed with hexane exhibits much less radial expansion (5 μm) relative to a steerable tip without the coating (20 μm).

to luer lock connectors. This process involves connecting polyimide microtubing (Microlumen, Oldsmar, FL, USA) with the hyperelastic material steerable tip. Pebax 3533 (Nordson Medical, Huntington Beach, CA, USA), selected for its flexibility and durability, was reflowed over the polyimide–Dragon Skin interface to complete the bonding process. The ratio of polyamide to polyether defines the material's stiffness or durometer. Pebax tube segments of increasing durometer hardness were telescopically connected via standard reflow procedures to obtain full-length (160 cm) catheters. The transitional stiffness design was selected to comply with clinical requirements, where lower durometer materials (Pebax 3533 and Pebax 4533) are used closer to the cerebral arteries, intermediate durometer materials (Pebax 5033 and Pebax 6233) are used in the cardiovascular region, and higher durometer materials (Pebax 7233) are used closer to the insertion region at the femoral artery. Although general factors relating to guide catheter selection often come down to personal choice or experience, generally desirable properties in a catheter are a soft atraumatic distal end, a sturdy proximal shaft for support, and multiply graded transitions in rigidity from the proximal to distal ends (*116*). In commercially available catheters, the lengths and durometer hardness of each section are proprietary. Various systems have been proposed in research (*117*), some including 12 segments (*118*), others specifically analyzing respective lengths of stiff and soft sections at the tip (*119*). However, because of subjective preferences and anatomical and clinical case variations, no gold standard exists for lengths of the transitional rigidity zones. Using the representative lengths of the ICA, CCA, brachiocephalic trunk, descending aorta, abdominal aorta, common iliac, and external iliac artery sections of the catheter were assembled. These were iteratively tested in the ex vivo silicone model, and clinician feedback was used to modify the lengths to improve pushability while maintaining a soft distal end. The final design had Pebax 3533 (10 cm), Pebax 4533 (12 cm), Pebax 5033 (15 cm), Pebax 6233 (23 cm), and Pebax 7233 (100 cm).

### Hydrophilic coating protocol

The assembled microcatheter is Pebax tubing tethered to a hyperelastic material tip. An internal and external hydrophilic coating (ON-470, Aculon Inc., San Diego, CA, USA) was applied to coat the catheter via submerged dip coating. To obtain a clear passageway in the central lumen, compressed air was injected at 2 psi for 2 min after dipping.

### Experimental characterization of the steerable tip

The performance of the steerable tip was quantified through measurements of the tip curvature versus input pressure over time. Combining imagery (FASTCAM Mini AX200, Photron, San Diego, CA, USA) with a high-precision microfluidics system (OB-1, Elveflow, Paris, France) and custom image postprocessing (MATLAB R2020a, MathWorks, Natick, MA, USA), the curvature of the tip was obtained as a function of the input pressure as shown in Fig. 3. The experiment was designed such that the Photron camera triggers recording in synchrony with the input pressure from the Elveflow system. The imposed pressure and camera frame rate were set to be equal at 50 Hz.

### One-to-one motion of the catheter

During surgical intervention, tip deflection requires timely response to the hand motions of the interventionist. The response time ($\tau$)

can be analytically estimated as $P = 1 - \exp\frac{-t}{\tau}$ (*120*). The hydraulic channel is a closed system between the input and the hyperelastic material tip. The transient response of the tip deflection to step changes in input pressure in fig. S1 shows that $\tau < 1$ s despite 1.6 m of connecting 50-μm-diameter microtubing between the two.

### Computational simulations

A finite element–based model was devised (ANSYS Inc., Canonsburg, PA, USA) to represent the geometrically nonlinear finite deformation of the hyperelastic, nonlinear stiffening material in the catheter tip to produce the results plotted in fig. S2. Because of the relatively low strains (<10%) induced in this application, a two-parameter Mooney-Rivlin model (*121*, *122*) was used to model the material properties. Hyperelastic constants $C_1$ and $C_2$ necessary for the model were separately extracted by conducting biaxial membrane tests on thin films (*91*). A manual element control with a reduced brick integration scheme and a linear tetrahedron mesh with adaptive sizing were used. Boundary conditions include a fixed face at the beginning of the steerable tip and a normal pressure applied within the hydraulic channel. To account for the changes in size and aspect ratio of the elements during the finite deformation of the tip structure, a nonlinear adaptive deformation scheme (*123*) was used to ensure convergence with the hyperelastic material.

### A representative ex vivo model of the vasculature with realistic cardiac flow

Anonymized CT angiogram DICOM images from a patient with representative vasculature tortuosity for the mean age group treated for intracranial aneurysms were segmented using 3DSlicer (*124*) to obtain the vasculature in a format suitable for 3D printing. A model of the vascular structure was 3D-printed with ABS (acrylonitrile butadiene styrene) plastic. The surface of the 3D-printed models was treated with an acetone vapor bath at 40°C for 30 min to obtain a smooth surface finish. The smoothed 3D model was dip-coated with eight layers of a translucent hyperelastic polymer (SORTA-clear 40, Smooth-On Inc., Macungie, PA USA), allowing a 24-hour cure time for each layer. The polymer-coated model was placed in an acetone bath to dissolve the ABS, leaving behind the ex vivo silicone model. The walls of the silicone model were rendered hydrophilic with a surface coating (ON-470, Aculon Inc., San Diego, CA, USA) to reduce the friction between the silicone model and the outer walls of the catheter and to mimic the lubricity of endothelial cells in the human vasculature.

The use of anonymized DICOM-formatted imagery to produce the vascular in-silicone model was conducted under University of California San Diego (UCSD) Institutional Review Board–approved protocol 171538, entitled "Prospective and retrospective observational study in human subjects undergoing radiology examinations for clinical care", most recently approved on 28 September 2019.

### Pulsatile flow using a blood flow analog

The ex vivo silicone model was connected to an external flow system (FlowTek 125, UnitedBiologics, Santa Ana, CA, USA) to generate pulsatile flow and pump a physician-verified blood analog (SLIP solution, UnitedBiologics, Santa Ana, CA, USA) to provide a representative validation model to mimic blood pumped by the heart. The pulsatile flow pump enables control of the pulse rate and flow rate. An immersion heater was used to maintain the blood flow analog at a temperature of 37°C (98.6°C) representative of the clinical environment. Because the silicone model is an isolated segmentation of the endovascular coiling arterial route, the flow rate through the aneurysm location was calibrated to achieve 50 ml/min prescribed by standard measurements of flow rates through cerebral arteries (*125*). The temperature of the blood analog was maintained at 37°C (98.6°F) using an immersion heater with thermostat to represent normal temperature of blood in vessels.

### Flow rate calibration

The pressure at the inlet of the ICA and exit of the PCOM (as shown in fig. S3) was measured using a high-resolution pressure sensor (2SMPP-03, OMRON, Kyoto, Japan) (*126*) at different flow rates generated by the pulsatile flow pump. The pressure difference was used to compute the flow rate assuming laminar flow and therefore the validity of the Hagen-Poiseuille equation to represent the pressure drop–flow rate relationship. The Reynolds number is ~50 to 100, justifying the laminar flow assumption.

### Emulating neuroendovascular surgery, testing, and coil deployment in the ex vivo model

Using a female luer connector at the right femoral artery of the silicone model, a guide catheter (ENVOY XB 6F, Codman & Shurtleff Inc., Raynham, MA, USA) was inserted into the silicone model with its tip parked at the middle of the ICA. A rotating hemostatic valve (RHV) was connected to the Envoy hub, and the steerable microcatheter was advanced until the distal end of the Envoy. A second RHV was connected to the hub of the steerable catheter. Both the RHVs were connected to standard saline at a pressure of 300 mmHg to set up the flush lines in line with standard endovascular neurosurgical protocols (*97*). The second RHV was used as the insertion point for the microguidewire (Synchro2, Stryker Neurovascular, Kalamazoo, MI, USA). Upon reaching the distal end, both the microguidewire and steerable microcatheter were advanced in tandem with the guidewire leading the way to the aneurysm. At the neck of the aneurysm location, the guidewire was retrieved and hydraulic actuation of the steerable catheter was used to engage active steering and place the distal end of the steerable tip into the dome of the aneurysm. Once the tip was positioned in the geometrical center of the aneurysm, the hydraulic channel was locked using a one-way stopcock to hold the steerable tip in a fixed position. Detachable coils [FC-6-20-3D, AXIUM PRIME detachable coils (frame), Medtronic, Irvine, CA, USA] were introduced through the steerable microcatheter's hub and deployed into the dome of the aneurysm.

### In vivo testing

A 6-Fr sheath was placed in the left femoral artery using the modified Seldinger technique (*98*). Under roadmap fluoroscopic guidance (Siemens Artis Zeego, PA, USA), a 5-Fr guide catheter (Guider Softip, Boston Scientific, MA, USA) was placed in the right CCA over a 889 μm wire (Glidewire, Terumo, CA, USA). A straight 355.6-μm microguidewire (Synchro2, Stryker Neurovascular, Kalamazoo, MI, USA) was inserted into the steerable microcatheter. The microguidewire and microcatheter were advanced to the distal end of the guide catheter in tandem. The 6-Fr sheath, 5-Fr guide catheter, and steerable microcatheter were flushed with continuously running saline using standard RHVs (Tuohy-Borst Y connector). The microguidewire was retrieved, the hydraulic steering engaged, and the steerable microcatheter was advanced to perform guidewire-free

navigation to access the ascending pharyngeal artery. After advancing the steerable portion of the microcatheter 25 mm into the ascending pharyngeal artery, the pressure in the hydraulic channel was gradually released, and the tip returned to its native curvature. The microcatheter was advanced beyond the radial center of the parotid artery, and then the relevant hydraulic channel was engaged to access to the parotid artery. The catheter was locked in this curvature and position, and platinum coils (FC-6-20-3D, AXIUM PRIME) were introduced.

### Animal care and use

This study was approved by the UCSD Animal Care and Use Committee–approved protocols S12204 (from 17 August 2016) and S13289 (from 15 March 2017), conforming to ARRIVE guidelines 2.0 (National Centre for the Replacement, Refinement and Reduction of Animals in Research) (*127*). The work was conducted by A.K. and his fellows in the UCSD Medical Education and Telemedicine Building's Center for Future Surgery surgical theater rooms in La Jolla, CA. J.F. and team were present for all surgical laboratory sessions. A living porcine model was selected for this study for the following reasons:

1) Swine to be used in this study represent a published model for aneurysm treatment, stent, and embolectomy device testing.

2) From an anatomical and physiological perspective, the circulatory system of the swine is an acceptable approximation of the circulatory system of humans, and as a result, the test system that is being used in this study is one that is used regularly for testing products intended for human use.

3) Historically, the swine has proved to be an excellent model for cerebral vascular evaluations and therapy.

4) The experience of the laboratory with this model allows for more valid judgment concerning model-related complications.

5) Ex vivo and computational models are inadequate to represent the complexity of the circulatory system in swine (and humans) in conducting procedures to treat aneurysms.

These animals were and are being used in neurointerventional surgery training according to the approved protocols. A.K. and his fellows used a broad variety of microguidewires, microcatheters, stents, and other tools to treat aneurysms, stroke, and other neurological disorders in the porcine model. The prototype devices produced from our work were integrated and approved into this protocol, testing the utility of the steerable microcatheter prototypes alongside the use of these other tools. Because the animals are already being used for training purposes in this terminal protocol, the principal concerns are the number of animals required to obtain statistically relevant usage data and the procedures to be used for these prototypes to avoid discomfort, distress, pain, and injury.

For this study, the prototype devices were trialed in two skeletally mature (47-kg) adult female *Sus scrofa YMP* (Yucatan miniature pigs), one each in two separate sessions. No control pigs were used. The minimum number of pigs, i.e., two, facilitated assessment of the prototype devices. These pigs were randomly and blindly selected from 16 healthy swine that were housed and maintained as a single species group at the UCSD livestock facility on the La Jolla campus under the supervision of veterinary staff according to BVA-AWF (British Veterinary Association–Animal Welfare Foundation) guidelines and United States Department of Agriculture regulations (reg. no. 93-R-0437). No exclusions were made. The animals were individually housed but with social contact with conspecifics whenever possible. Indoor or sheltered outdoor housing was provided of an appropriate size based on weight. Water was provided ad libitum at all times, and nutritionally complete pelleted feed metered per the individual animal's weight was provided daily. Enrichment materials that are sanitizable (hard balls, plastic chains, polyvinyl chloride pieces, and nylabones) were provided in the individual animal housing. Those animals that were isolated had daily positive interaction with humans.

The animals were transported to the surgical rooms on the day of the planned laboratory by trained veterinary staff in approved rolling transport pens. Because it was an acute study, no animals were returned to the housing; the pigs were euthanized upon session completion. Food was withheld at midnight before the operation date. Water was not restricted. A preanesthetic cocktail of ketamine (33 mg/kg), xylasine (2 mg/kg), and atropine (0.05 mg/kg) was given via intramuscular injection. An angiocatheter was then inserted percutaneously into a large ear vein and anesthetic induction was then achieved with propofol (2.4 mg/kg; titrated to negative jaw tone). Intubation followed with ventilation and administration of general anesthesia (inhaled isoflurane, 1 to 2%). The ventilator exhaust was scavenged with an external exhaust vacuum system. The electrocardiogram and blood oxygen and carbon dioxide percentages were continuously monitored, and a drip infusion of lactated ringers maintained hydration. Any movement, increase in heart rate or jaw tone, pupil reflex, or response to toe pinch was interpreted as a need for additional anesthesia. The operating room table was heated with a warm water pad. General anesthesia was maintained with inhalational isoflurane.

The invasive procedure began only after adequate sedation, anesthesia, and monitoring was established, requiring 30 min or less. The subject was placed in the supine position to permit shaving, preparation, and draping of the groin. The eyes of the animal were lubricated with a lubricant eye ointment. Femoral artery puncture was performed, and the introducer sheaths were placed in the left and right femoral arteries. A 6- to 7-F guide catheter was placed through the introducer sheath for navigation, device placement procedures, and contrast media injection. A RHV with side arm was attached to the end of the guide catheter, and the side arm was connected to a continuous flushing system. The prototype steerable microcatheter was then introduced and advanced to the CCA and related arteries for navigation and wire deployment under fluoroscopic (x-ray) guidance. All procedures occurred under the direct supervision of board-certified endovascular interventional specialists. The sessions were about 4 hours in duration and were performed while maintaining animal anesthesia throughout: The animal was not allowed to recover consciousness.

The subjects did not exhibit signs of pain or distress during the sessions. If they had exhibited such signs, anesthetic and analgesic compounds would have been administered by veterinary staff present for the entire session duration. The animals did not become hemodynamically unstable as determined by increased heart rate and decreased blood pressure. If this had happened, then the lactated ringers infusion rate would have been increased to meet the animal's volume requirements. The animals were euthanized at the completion of the procedure via intravenous administration of pentobarbital at 90 mg/kg. Confirmation of death was assured via flat-line electrocardiogram. The sessions were conducted under the supervision of certified staff from UCSD's veterinary services to ensure adherence to the guidelines established by the Panel on Euthanasia of the American Veterinary Medical Association.

## SUPPLEMENTARY MATERIALS

robotics.sciencemag.org/cgi/content/full/6/57/eabf0601/DC1
Text
Figs. S1 to S3
Movies S1 to S4

## REFERENCES AND NOTES


1. A. I. Qureshi, V. Janardhan, R. A. Hanel, G. Lanzino, Comparison of endovascular and surgical treatments for intracranial aneurysms: An evidence-based review. *Lancet Neurol.* **6**, 816–825 (2007).
2. G. J. E. Rinkel, M. Djibuti, A. Algra, J. Van Gijn, Prevalence and risk of rupture of intracranial aneurysms: A systematic review. *Stroke* **29**, 251–256 (1998).
3. M. H. Vlak, A. Algra, R. Brandenburg, G. J. Rinkel, Prevalence of unruptured intracranial aneurysms, with emphasis on sex, age, comorbidity, country, and time period: A systematic review and meta-analysis. *Lancet Neurol.* **10**, 626–636 (2011).
4. Brain Aneurysm Foundation, Brain aneurysm statistics (2020); https://bafound.org/about-brain-aneurysms/brain-aneurysm-basics/brain-aneurysm-statistics-and-facts/.
5. R. J. Singer, C. S. Ogilvy, G. Rordorf, Etiology, clinical manifestations, and diagnosis of aneurysmal subarachnoid hemorrhage (UpToDate, 2012).
6. R. D. Brown Jr., J. P. Broderick, Unruptured intracranial aneurysms: Epidemiology, natural history, management options, and familial screening. *Lancet Neurol.* **13**, 393–404 (2014).
7. D. O. Wiebers, J. C. Torner, I. Meissner, Impact of unruptured intracranial aneurysms on public health in the united states. *Stroke* **23**, 1416–1419 (1992).
8. S. Juvela, M. Porras, O. Heiskanen, Natural history of unruptured intracranial aneurysms: A long-term follow-up study. *J. Neurosurg.* **79**, 174–182 (1993).
9. S. Juvela, K. Poussa, H. Lehto, M. Porras, Natural history of unruptured intracranial aneurysms: A long-term follow-up study. *Stroke* **44**, 2414–2421 (2013).
10. R. Bonita, S. Thomson, Subarachnoid hemorrhage: Epidemiology, diagnosis, management, and outcome. *Stroke* **16**, 591–594 (1985).
11. J. W. Hop, G. J. Rinkel, A. Algra, J. van Gijn, Case-fatality rates and functional outcome after subarachnoid hemorrhage a systematic review. *Stroke* **28**, 660–664 (1997).
12. A. Keedy, An overview of intracranial aneurysms. *McGill J. Med.* **9**, 141 (2006).
13. G. Guglielmi, F. Viñuela, J. Dion, G. Duckwiler, Electrothrombosis of saccular aneurysms via endovascular approach: Part 2: Preliminary clinical experience. *J. Neurosurg.* **75**, 8–14 (1991).
14. G. Guglielmi, F. Viñuela, G. Duckwiler, J. Dion, P. Lylyk, A. Berenstein, C. Strother, V. Graves, V. Halbach, D. Nichols, N. Hopkins, R. Ferguson, I. Sepetka, Endovascular treatment of posterior circulation aneurysms by electrothrombosis using electrically detachable coils. *J. Neurosurg.* **77**, 515–524 (1992).
15. G. Guglielmi, History of endovascular endosaccular occlusion of brain aneurysms: 1965–1990. *Interv. Neuroradiol.* **13**, 217–224 (2007).
16. B. G. Thompson, R. D. Brown, S. Amin-Hanjani, J. P. Broderick, K. M. Cockroft, E. S. Connolly Jr., G. R. Duckwiler, C. C. Harris, V. J. Howard, S. C. C. Johnston, P. M. Meyers, A. Molyneux, C. S. Ogilvy, A. J. Ringer, J. Torner; American Heart Association Stroke Council; Council on Cardiovascular and Stroke Nursing, and Council on Epidemiology and Prevention; American Heart Association; American Stroke Association, [Guidelines for the management of patients with unruptured intracranial aneurysms: A guideline for healthcare professionals from the American Heart Association/American Stroke Association]. *Stroke* **46**, 2368–2400 (2015).
17. A. J. Molyneux, R. S. Kerr, J. Birks, N. Ramzi, J. Yarnold, M. Sneade, J. Rischmiller; ISAT Collaborators, Risk of recurrent subarachnoid haemorrhage, death, or dependence and standardised mortality ratios after clipping or coiling of an intracranial aneurysm in the International Subarachnoid Aneurysm Trial (ISAT): Long-term follow-up. *Lancet Neurol.* **8**, 427–433 (2009).
18. A. J. Molyneux, J. Birks, A. Clarke, M. Sneade, R. S. Kerr, The durability of endovascular coiling versus neurosurgical clipping of ruptured cerebral aneurysms: 18 year follow-up of the UK cohort of the International Subarachnoid Aneurysm Trial (ISAT). *Lancet* **385**, 691–697 (2015).
19. P. Bloss, W. Rothe, P. Wünsche, C. Werner, A. Rothe, G. D. Kneissl, W. Burger, E. Rehberg, Investigations of the pushability behavior of cardiovascular angiographic catheters. *Biomed. Mater. Eng.* **13**, 327–343 (2003).
20. D. W. Muller, R. Spina, Guiding catheters and wires, in *Cardiovascular Catheterization and Intervention: A Textbook of Coronary, Peripheral, and Structural Heart Disease* (CRC Press, ed. 1, 2010).
21. A. Ali, A. Sakes, E. A. Arkenbout, P. Henselmans, R. van Starkenburg, T. Szili-Torok, P. Breedveld, Catheter steering in interventional cardiology: Mechanical analysis and novel solution. *Proc. Inst. Mech. Eng. H* **233**, 1207–1218 (2019).
22. J. Himpens, G. Leman, G. B. Cadiere, Telesurgical laparoscopic cholecystectomy. *Surg. Endosc.* **12**, 1091 (1998).
23. A. Simorov, R. S. Otte, C. M. Kopietz, D. Oleynikov, Review of surgical robotics user interface: What is the best way to control robotic surgery? *Surg. Endosc.* **26**, 2117–2125 (2012).
24. D. Q. Larkin, T. G. Cooper, C. J. Mohr, D. J. Rosa, Minimally invasive surgical system, U.S. Patent 9,060,678 (2015).
25. B. S. Peters, P. R. Armijo, C. Krause, S. A. Choudhury, D. Oleynikov, Review of emerging surgical robotic technology. *Surg. Endosc.* **32**, 1636–1655 (2018).
26. Y. Hu, W. Li, L. Zhang, G.-Z. Yang, Designing, prototyping, and testing a flexible suturing robot for transanal endoscopic microsurgery. *IEEE Robot. Autom. Lett.* **4**, 1669–1675 (2019).
27. M. Madou, J. Florkey, From batch to continuous manufacturing of microbiomedical devices. *Chem. Rev.* **100**, 2679–2692 (2000).
28. M. J. Madou, *Fundamentals of Microfabrication and Nanotechnology* (CRC Press, 2011).
29. M. J. Madou, *Fundamentals of Microfabrication: The Science of Miniaturization* (CRC Press, 2018).
30. Y. Fu, H. Liu, W. Huang, S. Wang, Z. Liang, Steerable catheters in minimally invasive vascular surgery. *Int. J. Med. Robot.* **5**, 381–391 (2009).
31. G.-Z. Yang, J. Bellingham, P. E. Dupont, P. Fischer, L. Floridi, R. Full, N. Jacobstein, V. Kumar, M. McNutt, R. Merrifield, B. J. Nelson, B. Scassellati, M. Taddeo, R. Taylor, M. Veloso, Z. L. Wang, R. Wood, The grand challenges of *Science Robotics*. *Sci. Robot.* **3**, eaar7650 (2018).
32. M. Sitti, D. S. Wiersma, Pros and cons: Magnetic versus optical microrobots. *Adv. Mater.* **32**, 1906766 (2020).
33. H. Tillander, Magnetic guidance of a catheter with articulated steel tip. *Acta Radiol.* **35**, 62–64 (1951).
34. W. S. Trimmer, Microrobots and micromechanical systems. *Sens. Actuat.* **19**, 267–287 (1989).
35. S. Spearing, Micro devices and micro systems, materials for, in *Encyclopedia of Materials: Science and Technology*, K. J. Buschow, R. W. Cahn, M. C. Flemings, B. Ilschner, E. J. Kramer, S. Mahajan, P. Veyssiere, Eds. (Elsevier, 2001), pp. 5580–5587.
36. S. L. Charreyron, B. Zeydan, B. J. Nelson, Shared control of a magnetic microcatheter for vitreoretinal targeted drug delivery, in *Proceedings of the 2017 IEEE International Conference on Robotics and Automation (ICRA)*, Singapore, 29 May to 3 June 2017.
37. M. S. Choi, Y.-S. Oh, S. W. Jang, J. H. Kim, W. S. Shin, H.-J. Youn, W. S. Jung, M. Y. Lee, K. B. Seong, Comparison of magnetic navigation system and conventional method in catheter ablation of atrial fibrillation: Is magnetic navigation system is more effective and safer than conventional method? *Korean Circ. J.* **41**, 248–252 (2011).
38. N. Gudino, J. A. Heilman, J. J. Derakhshan, J. L. Sunshine, J. L. Duerk, M. A. Griswold, Control of intravascular catheters using an array of active steering coils. *Med. Phys.* **38**, 4215–4224 (2011).
39. C. Chautems, A. Tonazzini, Q. Boehler, S. H. Jeong, D. Floreano, B. J. Nelson, Magnetic continuum device with variable stiffness for minimally invasive surgery. *Adv. Intell. Syst.*, 1900086 (2019).
40. H.-W. Huang, M. S. Sakar, A. J. Petruska, S. Pané, B. J. Nelson, Soft micromachines with programmable motility and morphology. *Nat. Commun.* **7**, 12263 (2016).
41. Y. Zhu, D. S. Antao, R. Xiao, E. N. Wang, Real-time manipulation with magnetically tunable structures. *Adv. Mater.* **26**, 6442–6446 (2014).
42. Y. Kim, G. A. Parada, S. Liu, X. Zhao, Ferromagnetic soft continuum robots. *Sci. Robot.* **4**, eaax7329 (2019).
43. L. Di Biase, T. S. Fahmy, D. Patel, R. Bai, K. Civello, O. M. Wazni, M. Kanj, C. S. Elayi, C. K. Ching, M. Khan, L. Popova, R. A. Schweikert, J. E. Cummings, J. D. Burkhardt, D. O. Martin, M. Bhargava, T. Dresing, W. Saliba, M. Arruda, A. Natale, Remote magnetic navigation: Human experience in pulmonary vein ablation. *J. Am. Coll. Cardiol.* **50**, 868–874 (2007).
44. A. Arya, G. Hindricks, P. Sommer, Y. Huo, A. Bollmann, T. Gaspar, K. Bode, D. Husser, H. Kottkamp, C. Piorkowski, Long-term results and the predictors of outcome of catheter ablation of atrial fibrillation using steerable sheath catheter navigation after single procedure in 674 patients. *Europace* **12**, 173–180 (2009).
45. D. Filgueiras-Rama, A. Estrada, J. Shachar, S. Castrejón, D. Doiny, M. Ortega, E. Gang, J. L. Merino, Remote magnetic navigation for accurate, real-time catheter positioning and ablation in cardiac electrophysiology procedures. *J. Vis. Exp.*, 3658 (2013).
46. H. Rafii-Tari, C. J. Payne, G.-Z. Yang, Current and emerging robot-assisted endovascular catheterization technologies: A review. *Ann. Biomed. Eng.* **42**, 697–715 (2014).
47. W. F. Muller, Spring guide manipulator, U.S. Patent 3,452,740 (1969).
48. J. G. Hammerslag, G. R. Hammerslag, Steerable angioplasty device, U.S. Patent 4,921,482 (1990).
49. B. Avitall, Catheter deflection control, U.S. Patent 5,441,483 (1995).
50. D. Stevens-Wright, M. Russo, P. Nielsen, P. Bertram, Actuator for use with steerable catheter, U.S. Patent 5,462,527 (1995).
51. W. Feng, C. Chi, H. Wang, K. Wang, X. ye, S. Guo, Highly precise catheter driving mechanism for intravascular neurosurgery, in *Proceedings of the 2006 IEEE International Conference on Mechatronics and Automation*, IEEE, Luoyang, China, 25 to 28 June 2006.
52. X. Guo, T. T. Tegg, R. E. Stehr, Deflectable catheter with distal deflectable segment, U.S. Patent 7,985,215 (2011).

53. J. R. Watson, Asymmetric dual directional steerable catheter sheath, U.S. Patent 8,500,733 (2013).
54. M. Konings, T. Van Leeuwen, W. T. M. Mali, M. Viergever, Torsion measurement of catheters using polarized light in a single glass fibre. *Phys. Med. Biol.* **43**, 1049 (1998).
55. I. M. Kelly, C. S. Boyd, Buckling of the tethering catheter causes migration of a temporary caval filter to the right atrium. *Clin. Radiol.* **54**, 398–401 (1999).
56. M. D. Olson, N. Phreaner, J. L. Schuller, D. T. Nguyen, D. F. Katz, R. G. Aleong, W. S. Tzou, R. Sung, P. D. Varosy, W. H. Sauer, Effect of catheter movement and contact during application of radiofrequency energy on ablation lesion characteristics. *J. Interv. Card. Electrophysiol.* **38**, 123–129 (2013).
57. R. A. Caldwell, J. E. Woodell, S. P. Ho, S. W. Shalaby, T. Boland, E. M. Langan, M. Laberge, In vitro evaluation of phosphonylated low-density polyethylene for vascular applications. *J. Biomed. Mater. Res.* **62**, 514–524 (2002).
58. J. Bismuth, E. Kashef, N. Cheshire, A. B. Lumsden, Feasibility and safety of remote endovascular catheter navigation in a porcine model. *J. Endovasc. Ther.* **18**, 243–249 (2011).
59. P. Généreux, J. G. Webb, L. G. Svensson, S. K. Kodali, L. F. Satler, W. F. Fearon, C. J. Davidson, A. C. Eisenhauer, R. R. Makkar, G. W. Bergman, V. Babaliaros, J. E. Bavaria, O. C. Velazquez, M. R. Williams, I. Hueter, K. Xu, M. B. Leon; PARTNER Trial Investigators, Vascular complications after transcatheter aortic valve replacement: Insights from the partner (placement of aortic transcatheter valve) trial. *J. Am. Coll. Cardiol.* **60**, 1043–1052 (2012).
60. R. West, G. Ellis, N. Brooks, Complications of diagnostic cardiac catheterisation: Results from a confidential inquiry into cardiac catheter complications. *Heart* **92**, 810–814 (2006).
61. C.-H. Yun, L. Y. Yeo, J. R. Friend, B. Yan, Multi-degree-of-freedom ultrasonic micromotor for guidewire and catheter navigation: The neuroglide actuator. *Appl. Phys. Lett.* **100**, 164101 (2012).
62. X.-Z. Chen, J.-H. Liu, M. Dong, L. Müller, G. Chatzipirpiridis, C. Hu, A. Terzopoulou, H. Torlakcik, X. Wang, F. Mushtaq, J. Puigmartí-Luis, Q. D. Shen, B. J. Nelson, S. Pané, Magnetically driven piezoelectric soft microswimmers for neuron-like cell delivery and neuronal differentiation. *Mater. Horiz.* **6**, 1512–1516 (2019).
63. M. De Volder, D. Reynaerts, Pneumatic and hydraulic microactuators: A review. *J. Micromech. Microeng.* **20**, 043001 (2010).
64. D. Rus, M. T. Tolley, Design, fabrication and control of soft robots. *Nature* **521**, 467–475 (2015).
65. C. Laschi, B. Mazzolai, M. Cianchetti, Soft robotics: Technologies and systems pushing the boundaries of robot abilities. *Sci. Robot.* **1**, eaah3690 (2016).
66. P. Polygerinos, N. Correll, S. A. Morin, B. Mosadegh, C. D. Onal, K. Petersen, M. Cianchetti, M. T. Tolley, R. F. Shepherd, Soft robotics: Review of fluid-driven intrinsically soft devices; manufacturing, sensing, control, and applications in human-robot interaction. *Adv. Eng. Mater.* **19**, 1700016 (2017).
67. G. M. Whitesides, Soft robotics. *Angew. Chem. Int. Ed.* **57**, 4258–4273 (2018).
68. G. Dogangil, B. Davies, F. Rodriguez y Baena, A review of medical robotics for minimally invasive soft tissue surgery. *Proc. Inst. Mech. Eng. H* **224**, 653–679 (2010).
69. V. Vitiello, S.-L. Lee, T. P. Cundy, G.-Z. Yang, Emerging robotic platforms for minimally invasive surgery. *IEEE Rev. Biomed. Eng.* **6**, 111–126 (2013).
70. M. Cianchetti, T. Ranzani, G. Gerboni, T. Nanayakkara, K. Althoefer, P. Dasgupta, A. Menciassi, Soft robotics technologies to address shortcomings in today's minimally invasive surgery: The stiff-flop approach. *Soft Robot.* **1**, 122–131 (2014).
71. C. Bergeles, G.-Z. Yang, From passive tool holders to microsurgeons: Safer, smaller, smarter surgical robots. *IEEE Trans. Biomed. Eng.* **61**, 1565–1576 (2014).
72. S. Fusco, M. S. Sakar, S. Kennedy, C. Peters, R. Bottani, F. Starsich, A. Mao, G. A. Sotiriou, S. Pané, S. E. Pratsinis, D. Mooney, B. J. Nelson, An integrated microrobotic platform for on-demand, targeted therapeutic interventions. *Adv. Mater.* **26**, 952–957 (2014).
73. D.-H. Kim, N. Lu, R. Ghaffari, Y.-S. Kim, S. P. Lee, L. Xu, J. Wu, R.-H. Kim, J. Song, Z. Liu, J. Viventi, B. de Graff, S.-M. Won, Y. Huang, B. Litt, A. J. Rogers, Materials for multifunctional balloon catheters with capabilities in cardiac electrophysiological mapping and ablation therapy. *Nat. Mater.* **10**, 316–323 (2011).
74. E. T. Roche, M. A. Horvath, I. Wamala, A. Alazmani, S.-E. Song, W. Whyte, Z. Machaidze, C. J. Payne, J. C. Weaver, G. Fishbein, J. Kuelbler, N. V. Vasilyev, D. J. Mooney, F. A. Pigula, C. J. Walsh, Soft robotic sleeve supports heart function. *Sci. Transl. Med.* **9**, eaaf3925 (2017).
75. K. Suzumori, S. Iikura, H. Tanaka, Flexible microactuator for miniature robots, in *Proceedings of the IEEE Micro Electro Mechanical Systems* (IEEE, 1991), pp, 204–209.
76. K. Suzumori, S. Iikura, H. Tanaka, Applying a flexible microactuator to robotic mechanisms. *IEEE Control Syst.* **12**, 21–27 (1992).
77. K. Suzumori, A. Koga, H. Riyoko, Microfabrication of integrated FMAS using stereo lithography, in *Proceedings of the Micro Electro Mechanical Systems An Investigation of Micro Structures, Sensors, Actuators, Machines and Robotic Systems* (IEEE, 1994), pp. 136–141.
78. K. Ikuta, H. Ichikawa, K. Suzuki, Safety-active catheter with multiple-segments driven by micro-hydraulic actuators, in *International Conference on Medical Image Computing and Computer-Assisted Intervention— MICCAI 2002*, T. Dohi, R. Kikinis, Eds. (Springer, Berlin, Heidelberg), pp. 182–191.
79. Y. Haga, Y. Muyari, T. Mineta, T. Matsunaga, H. Akahori, M. Esashi, Small diameter hydraulic active bending catheter using laser processed super elastic alloy and silicone rubber tube, in *Proceedings of the 2005 3rd IEEE/EMBS Special Topic Conference on Microtechnology in Medicine and Biology* (IEEE, 2005), pp. 245–248.
80. Z. Galel, Catheter steerable by directional jets with remotely controlled closures, U.S. Patent 5,476,100 (1995).
81. J. Paek, I. Cho, J. Kim, Microrobotic tentacles with spiral bending capability based on shape-engineered elastomeric microtubes. *Sci. Rep.* **5**, 14151 (2015).
82. M. Wehner, R. L. Truby, D. J. Fitzgerald, B. Mosadegh, G. M. Whitesides, J. A. Lewis, R. J. Wood, An integrated design and fabrication strategy for entirely soft, autonomous robots. *Nature* **536**, 451–455 (2016).
83. C. Pappone, G. Vicedomini, F. Manguso, F. Gugliotta, P. Mazzone, S. Gulletta, N. Sora, S. Sala, A. Marzi, G. Augello, L. Livolsi, A. Santagostino, V. Santinelli, Robotic magnetic navigation for atrial fibrillation ablation. *J. Am. Coll. Cardiol.* **47**, 1390–1400 (2006).
84. S. R. Atmakuri, E. I. Lev, C. Alviar, E. Ibarra, A. E. Raizner, S. L. Solomon, N. S. Kleiman, Initial experience with a magnetic navigation system for percutaneous coronary intervention in complex coronary artery lesions. *J. Am. Coll. Cardiol.* **47**, 515–521 (2006).
85. W. Saliba, J. E. Cummings, S. Oh, Y. Zhang, T. N. Mazgalev, R. A. Schweikert, J. D. Burkhardt, A. Natale, Novel robotic catheter remote control system: Feasibility and safety of transseptal puncture and endocardial catheter navigation. *J. Cardiovasc. Electrophysiol.* **17**, 1102–1105 (2006).
86. Y. Matsumura, A. E. Kovalev, S. N. Gorb, Penetration mechanics of a beetle intromittent organ with bending stiffness gradient and a soft tip. *Sci. Adv.* **3**, eaao5469 (2017).
87. J. Friend, G. Tilvawala, Hydraulically driven surgical apparatus, U.S. Patent App. 16/334,695 (2019).
88. S. J. Schreiber, S. Gottschalk, M. Weih, A. Villringer, J. M. Valdueza, Assessment of blood flow velocity and diameter of the middle cerebral artery during the acetazolamide provocation test by use of transcranial doppler sonography and mr imaging. *Am. J. Neuroradiol.* **21**, 1207–1211 (2000).
89. P. Huber, J. Handa, Effect of contrast material, hypercapnia, hyperventilation, hypertonic glucose and papaverine on the diameter of the cerebral arteries: Angiographic determination in man. *Invest. Radiol.* **2**, 17–32 (1967).
90. H. Henkes, E. Miloslavski, S. Lowens, J. Reinartz, T. Liebig, D. Kühne, Treatment of intracranial atherosclerotic stenoses with balloon dilatation and self-expanding stent deployment (wingspan). *Neuroradiology* **47**, 222–228 (2005).
91. T. Gopesh, J. Friend, Facile analytical extraction of the hyperelastic constants for the two-parameter Mooney–Rivlin model from experiments on soft polymers. *Soft Robot.* 10.1089/soro.2019.0123 , (2020).
92. L. Peeling, D. Fiorella, Balloon-assisted guide catheter positioning to overcome extreme cervical carotid tortuosity: Technique and case experience. *J. Neurointerv. Surg.* **6**, 129–133 (2014).
93. B. N. Persson, O. Albohr, U. Tartaglino, A. Volokitin, E. Tosatti, On the nature of surface roughness with application to contact mechanics, sealing, rubber friction and adhesion. *J. Phys. Condens. Matter* **17**, R1 (2004).
94. A. S. Miranpuri, C. M. Nickele, E. Akture, K. Royalty, D. B. Niemann, Neuroangiography simulation using a silicone model in the angiography suite improves trainee skills. *J. Neurointerv. Surg.* **6**, 561–564 (2014).
95. P. Narra, J. Kuban, L. E. Grandpre, J. Singh, J. Barrero, A. Norbash, Videoscopic phantom-based angiographic simulation: Effect of brief angiographic simulator practice on vessel cannulation times. *J. Vasc. Interv. Radiol.* **20**, 1215–1223 (2009).
96. S. Konakondla, R. Fong, C. M. Schirmer, Simulation training in neurosurgery: Advances in education and practice. *Adv. Med. Educ. Pract.* **8**, 465–473 (2017).
97. S.-N. H. Khan, A. J. Ringer, *Handbook of Neuroendovascular Techniques* (Springer, 2017).
98. S. I. Seldinger, Catheter replacement of the needle in percutaneous arteriography: A new technique. *Acta Radiol.* **39**, 368–376 (1953).
99. O. Diaz, L. Rangel-Castilla, Endovascular treatment of intracranial aneurysms. *Handb. Clin. Neurol.* **136**, 1303–1309 (2016).
100. Medical Advisory Secretariat, Coil embolization for intracranial aneurysms: An evidence-based analysis. *Ont. Health Technol. Assess. Ser.* **6**, 1–114 (2006).
101. L. Pierot, A. K. Wakhloo, Endovascular treatment of intracranial aneurysms: Current status. *Stroke* **44**, 2046–2054 (2013).
102. R. Khatri, S. A. Chaudhry, G. J. Rodriguez, M. F. K. Suri, S. M. Cordina, A. I. Qureshi, Frequency and factors associated with unsuccessful lead (first) coil placement in patients undergoing coil embolization of intracranial aneurysms. *Neurosurgery* **72**, 452–458 (2013).
103. L. Elijovich, R. T. Higashida, M. T. Lawton, G. Duckwiler, S. Giannotta, S. C. Johnston; Cerebral Aneurysm Rerupture After Treatment (CARAT) Investigators, Predictors and outcomes of intraprocedural rupture in patients treated for ruptured intracranial aneurysms: The CARAT study. *Stroke* **39**, 1501–1506 (2008).

104. D. Kocur, N. Przybyłko, P. Bażowski, J. Baron, Rupture during coiling of intracranial aneurysms: Predictors and clinical outcome. *Clin. Neurol. Neurosurg.* **165**, 81–87 (2018).
105. R. Blanc, M. Piotin, C. Mounayer, L. Spelle, J. Moret, Direct cervical arterial access for intracranial endovascular treatment. *Neuroradiology* **48**, 925–929 (2006).
106. D. B. Orbach, C. Stamoulis, K. J. Strauss, J. Manchester, E. R. Smith, R. M. Scott, N. Lin, Neurointerventions in children: Radiation exposure and its import. *AJNR Am. J. Neuroradiol.* **35**, 650–656 (2014).
107. E. N. Kahn, J. J. Gemmete, N. Chaudhary, B. G. Thompson, K. Chen, E. G. Christodoulou, A. S. Pandey, Radiation dose reduction during neurointerventional procedures by modification of default settings on biplane angiography equipment. *J. NeuroInterv. Surg.* **8**, 819–823 (2015).
108. M. S. Pearl, C. Torok, J. Wang, E. Wyse, M. Mahesh, P. Gailloud, Practical techniques for reducing radiation exposure during cerebral angiography procedures. *J. Neurointerv. Surg.* **7**, 141–145 (2015).
109. J. M. Tobis, I. Abudayyeh, New devices and technology in interventional cardiology. *J. Cardiol.* **65**, 5–16 (2015).
110. S. Hascoet, A. Fraisse, M. Elbaz, Successful percutaneous transcatheter patent foramen ovale closure through the right internal jugular vein using a steerable catheter. *Catheter. Cardiovasc. Interv.* **82**, E598–E602 (2013).
111. F. Maisano, H. Vanermen, J. Seeburger, M. Mack, V. Falk, P. Denti, M. Taramasso, O. Alfieri, Direct access transcatheter mitral annuloplasty with a sutureless and adjustable device: Preclinical experience. *Eur. J. Cardiothorac. Surg.* **42**, 524–529 (2012).
112. M. Nounou, A. Harrison, M. Kern, A novel technique using a steerable guide catheter to successfully deliver an amplatzer septal occluder to close an atrial septal defect. *Catheter. Cardiovasc. Interv.* **72**, 994–997 (2008).
113. K. Tiroch, M. Vorpahl, M. Seyfarth, Novel mitral clipping technique overcoming extreme atrial dilatation. *Catheter. Cardiovasc. Interv.* **84**, 606–609 (2014).
114. J. Joseph, K. C. K. Wong, M. R. Ginks, Y. Bashir, T. R. Betts, K. Rajappan, Steerable sheath technology in the ablation of atrial fibrillation. *Recent Pat. Cardiovasc. Drug Discov.* **8**, 171–177 (2013).
115. J. Moret, C. Cognard, A. Weill, L. Castaings, A. Rey, Reconstruction technic in the treatment of wide-neck intracranial aneurysms. Long-term angiographic and clinical results. Apropos of 56 cases. *J. Neuroradiol.* **24**, 30–44 (1997).
116. M. S. Noone, A. H. Dunfee, M. S. Poole, Multiple segment catheter and method of fabrication, U.S. Patent 6,591,472 (2003).
117. F. K. Hui, A. J. Schuette, A. M. Spiotta, J. Yim, N. Obuchowski, P. A. Rasmussen, M. S. Hussain, C. M. Cawley, J. E. Dion, F. C. Tong, Flexible tip guides and intermediate catheters: Two center experience and a proposed taxonomy. *J. Neurointerv. Surg.* **6**, 618–623 (2014).
118. G. P. Colby, L.-M. Lin, R. Xu, N. Beaty, M. T. Bender, B. Jiang, J. Huang, R. J. Tamargo, A. L. Coon, Utilization of a novel, multi-durometer intracranial distal access catheter: Nuances and experience in 110 consecutive cases of aneurysm flow diversion. *Interv. Neurol.* **6**, 90–104 (2017).
119. C. Chautems, A. Tonazzini, D. Floreano, B. J. Nelson, A variable stiffness catheter controlled with an external magnetic field, in *Proceedings of the 2017 IEEE/RSJ International Conference on Intelligent Robots and Systems (IROS)*, IEEE, Vancouver, BC, Canada, 24 to 28 September 2017.
120. K. Nakamura, M. Kurosawa, H. Kurebayashi, S. Ueha, An estimation of load characteristics of an ultrasonic motor by measuring transient responses. *IEEE Trans. Ultrason. Ferroelectr. Freq. Control* **38**, 481–485 (1991).
121. M. Mooney, A theory of large elastic deformation. *J. Appl. Phys.* **11**, 582–592 (1940).
122. R. S. Rivlin, D. W. Saunders, Large elastic deformations of isotropic materials VII. Experiments on the deformation of rubber. *Philos. Trans. R. Soc. Lond. A Math. Phys. Sci.* **243**, 251–288 (1951).
123. G. R. Bhashyam, ANSYS mechanical—A powerful nonlinear simulation tool. *ANSYS Inc.* **1**, 39 (2002).
124. R. Kikinis, S. D. Pieper, K. G. Vosburgh, 3D slicer: A platform for subject-specific image analysis, visualization, and clinical support, in *Intraoperative Imaging and Image-Guided Therapy*, F. Jolesz, Ed. (Springer, 2014), pp. 277–289.
125. L. Zarrinkoob, K. Ambarki, A. Wåhlin, R. Birgander, A. Eklund, J. Malm, Blood flow distribution in cerebral arteries. *J. Cereb. Blood Flow Metab.* **35**, 648–654 (2015).
126. T. Gopesh, A. Camp, M. Unanian, J. Friend, R. N. Weinreb, Rapid and accurate pressure sensing device for direct measurement of intraocular pressure. *Transl. Vis. Sci. Technol.* **9**, 28 (2020).
127. N. Percie du Sert, V. Hurst, A. Ahluwalia, S. Alam, M. T. Avey, M. Baker, W. J. Browne, A. Clark, I. C. Cuthill, U. Dirnagl, M. Emerson, P. Garner, S. T. Holgate, D. W. Howells, N. A. Karp, S. E. Lazic, K. Lidster, C. J. MacCallum, M. Macleod, E. J. Pearl, O. H. Petersen, F. Rawle, P. Reynolds, K. Rooney, E. S. Sena, S. D. Silberberg, T. Steckler, H. Würbel, The ARRIVE guidelines 2.0: Updated guidelines for reporting animal research. *PLOS Biol.* **18**, e3000410 (2020).


**Acknowledgments:** We would like to thank S. Van Voorhis (David Schnurr Associates), Zeus Industrial Products, and Aculon Inc. for the support. We would also like to thank the staff at the UCSD Center for Future Surgery and T. Livingston (RT). J.F. wishes to dedicate this paper to the memory of his grandmother, D. Friend, who passed away in large part due to a cerebral aneurysm brought on by a medical misadventure. **Funding:** T.G. is grateful to the American Heart Association for grant 16PRE31430005 and the American-Australian Association Sir Keith Murdoch Scholarship in support of this project. We are grateful for funding provided by the American Heart Association's Innovative Project Award (19IPLOI34760705), the state of California's AB2664 Medical Entrepreneurship Education and Training Grant scheme, UCSD's Galvanizing Engineering in Medicine program, and the NIH via the University of California Center for Accelerated Innovation (NIH/NCATS UCSD CTRI 1UL1TR001442-01). **Author contributions:** J.F. devised the initial concept with B.Y. and designed the research, method, testing, and characterization techniques. T.G. designed and fabricated the device, devised the fabrication methods, and conducted image postprocessing, characterization, and analysis. T.G. and J.H.W. developed the representative ex vivo silicone model and flow setup. Ex vivo testing and feedback were provided by B.Y., D.S.-D., A.K., and A.N. The in vivo porcine test was conducted by T.G., J.H.W., D.S.-D., J.S.P., and A.K. T.G., J.H.W., D.S.-D., and J.F. wrote the paper. **Competing interests:** T.G. and J.F. are authors on a patent application US20190209811A1, titled "Hydraulically driven surgical apparatus" submitted by University of California, which covers design and manufacturing methods for the steerable catheter and control system (*87*). A.K. received options for serving as a medical board advisor to Ospitek as a consultant on inventory and patient tracking in outpatient surgery centers, which does not overlap with the research reported in this paper. A.K. is on the steering committee for the EMBOLISE trial for Medtronic; this trial is examining middle meningeal artery embolization for treating subdural hematoma; Medtronic is not involved in the research reported in this study and the EMBOLISE trial has no relevance to steerable catheter technology, although Medtronic does have an endovascular device portfolio. A.K. serves on the global advisory board of Cerenovus, the endovascular arm of Johnson and Johnson, receiving modest consulting income from the arrangement. Cerenovus and Johnson and Johnson are not involved in this paper's work nor is A.K.'s relationship connected in any way to this activity. **Data and materials availability:** All data needed to evaluate the conclusions in the paper are present in the paper or the Supplementary Materials. Any raw data, images, or video associated with this work may be obtained through the open access, UCSD Library-maintained Research Data Collection in the collection entitled "Data from: Soft robotic steerable microcatheter for the endovascular treatment of cerebral disorders" (https://doi.org/10.6075/J0R49QN8).

Submitted 2 October 2020
Accepted 26 July 2021
Published 18 August 2021
10.1126/scirobotics.abf0601

**Citation:** T. Gopesh, J. H. Wen, D. Santiago-Dieppa, B. Yan, J. S. Pannell, A. Khalessi, A. Norbash, J. Friend, Soft robotic steerable microcatheter for the endovascular treatment of cerebral disorders. *Sci. Robot.* **6**, eabf0601 (2021).

Science Robotics

# Soft robotic steerable microcatheter for the endovascular treatment of cerebral disorders

Tilvawala Gopesh, Jessica H. Wen, David Santiago-Dieppa, Bernard Yan, J. Scott Pannell, Alexander Khalessi, Alexander Norbash, and James Friend

*Sci. Robot.* **6** (57), eabf0601. DOI: 10.1126/scirobotics.abf0601







*Science Robotics* (ISSN 2470-9476) is published by the American Association for the Advancement of Science. 1200 New York Avenue NW, Washington, DC 20005. The title *Science Robotics* is a registered trademark of AAAS.